Polymer Components for Photonic Integrated Circuits

Aleksandrs Marinins

Abstract

Optical polymers are a subject of intense research and industry implementation for several decades. Nowadays, organic materials are widely utilized in microelectronic and optoelectronic businesses. Comparing to inorganic materials, optical polymers are inexpensive, easy to process and flexible enough to meet a broad range of application-specific requirements. These advantages allow a development of cost-efficient polymer photonic integrated circuits for on-chip optical communications, signal processing, sensing, etc. However, polymer platform suffers from some drawbacks, for example, low refractive index contrast between core and cladding. This limits light confinement in a core and, consequently, integrated polymer device miniaturization. Also, polymers lack active functionality like light emission, amplification, modulation, etc. In this work, we developed methods to improve a performance of integrated passive polymer waveguides and demonstrated active devices based on polymer waveguides doped with silicon quantum dots. Also, we present novel silicon nanocrystal/polymer hybrid optical materials for active applications.

In the integrated device part of this work, we demonstrate optical waveguides with enhanced performance. We report uniform high refractive index contrast of 57.5% in air-suspended SU-8 waveguides. After SiO_2 lower cladding removal, optical mode is well-confined and substrate leakage losses are eliminated. More of it, decreased radiation losses in curved waveguides allow low-loss bending with radii as small as 15 µm, which is far better than >100 µm for typical polymer waveguides. This approach provides high integration density and simplified photonic integrated circuit design. Another study shows a positive effect of thermal treatment on pedestal-standing acrylate waveguides. By heating slightly higher than polymer glass transition temperature, the viscosity decreases and reflows cracks and other surface roughness, minimizing scattering losses. Further heating reshapes initially rectangular waveguides into cylindrical ones yielding nearly negligible polarization dependent losses of <0.1 dB/cm, which is highly desirable for a proper circuit operation. When applied to polymer microring resonators, this treatment method enhances cavity Q factor more than 2 times. Considering polymers' high compatibility with different dopants, we fabricated and evaluated all-optical intensity modulator based on PMMA waveguides with silicon quantum dots encapsulated. Demonstrated active device shows a potential to become a low-cost kHz range switch in all-optical circuits.

We also developed and characterized novel hybrid optical materials. Here, photoluminescent Si nanocrystals are encapsulated into PMMA and OSTE polymers. Obtained nanocomposites show stable photoluminescence in visible and near-infrared region with high quantum efficiency. We achieved the highest up to date ~65% quantum yield for solid-state Si nanocrystal composites. Demonstrated materials are a step towards Si-based on-chip light sources and nonlinearity driven active devices.

Integrated devices and materials presented in this work enhance the performance and expand functionality of polymer PICs. The components described here can serve not only as elements of optical communication circuits, but also as building blocks for

on-chip sensing applications, microfluidics, optical memory, etc.

Keywords: integrated photonics, polymers, optical communications, microfabrication, optical waveguides, microring resonators, silicon, Si nanocrystals, photoluminescence.

Sammanfattning

Optiska polymermaterial är ett område för intensiv forskning som resulterat i ett flertal industriella tillämpningar de senaste årtionderna. I dagsläget används dessa organiska material standardmässigt inom mikroelektronik och optoelektronisk industri. I jämförelse med icke-organiska material, är polymermaterial billigare, lättare att använda samt tillräckligt flexibla för att kunna uppfylla kraven inom ett flertal olika specifika tillämpningar. Polymermaterialens fördelar gör att kostnadseffektiva fotoniska integrerade kretsar har kunnat utvecklats för användning inom optisk kommunikation, signalbehandling och mätningar.

Det finns dock ett antal nackdelar med optiska polymer material, där en är den låga kontrasten i brytningsindex mellan kärna och mantel, vilket begränsar ljusledarnas inneslutniongsförmåga och i sin tur hindrar miniatyrisering av de optisk komponenterna. En annan begränsning är bristen på aktiv funktionalitet i materialet såsom ljusemittering, förstärkning, modulering mm.

I denna avhandling presenterar vi metoder för att förbättra prestandan hos passiva integrerade optiska kretsar samt demonstrerar aktiva komponenter baserade på polymer vågledare dopade med kisel kvantpunkter. Utöver detta presentareas också nya optiska kompositmaterial baserade på kisel nanokristaller och optiska polymerer.

I kapitlen med integrerande optiska kretsar, visar vi på optiska vågledare med utökade prestanda såsom en hög, homogen brytningsindexkontrast på 57,5%, för luftburna SU-8 vågledare. Efter eliminering av SiO_2-mantel under vågledaren, fås en väl innesluten optisk mod med minimala läckageförluster. Vi visar även på minskade strålningsförluster som möjliggör böjda vågledare med radier ner till 15 μm, mycket bättre än de typiska värden på >100μm som är vanliga för andra polymera vågledare. Sammanlagt möjliggör detta en tätare integration och enklare design utav fotoniska integerade kretsar.

En annan studie i denna avhandling visar påde positiva effekter utav värmebehandling av piedistalstående vågledare i akrylatpolymer. Genom värmning till strax över glass temperaturen, minskar viskositeten och materialet flyter ut vilket fyller ut sprickor och jämnar ut andra ytdefekter, vilket ger minskade spridnings förluster. Ytterligare uppvärmning formar om de ursprungligen rektangulära vågledarna till cylidriska dito, vilket resulterar i närmast försumbara polarisationsberoende förluster, < 0.1dB/cm, en högst önskvärd egenskap hos välfungerande optiska kretsar. Samma process, applicerad på polymera ringresonatorer, ökade Q-värdet på kaviteterna mer än 2 gånger.

För att undersöka kompabiliteten mellan polymerer och olika dopämnen har vi tillverkat och utvärderat en heloptisk intensitetsmodulator baserade på en PMMA vågledare med inbäddade kisel kvantpunkter. Denna aktiva komponent visar sig ha en potential att bli en lågkostnads optisk switch med kHz prestanda för heloptiska kretsar.

Vi har också utvecklat och karakteriserat nya optiska hybridmaterial såsom fotoluminiscenta kisel nanokristaller inbäddade i PMMA och OSTE polymerer. Dessa

nanokompositer visar på stabil fotoluminiscens i det synliga och infraröda spektrat, med hög kvanteffektivitet. Vi uppnådde ett kvantutbyte på ca 65% vilket är det högsta värdet som rapporterats för kiselbaserade, nanokristall kompositer. Dessa material är ett steg på vägen mot kiselbaserade optiska kretsar med ljuskällor och ickelinjära, aktivt drivna komponenter. De integrerade kretsar och material som presenteras i detta arbete förbättrar prestanda och funktionen hos polymera fotoniska integrerade kretsar. De komponenter som beskrivs kan inte bara användas som delar i optiska kommunikationssytem utan även som byggblock inom chipbaserade sensorer, mikrofluidkomponenter och optisk minnen.

Acknowledgements

I am deeply grateful to all the people who inspired and guided me through doctoral studies.

First of all, I want to thank Prof. Sergei Popov, my supervisor, for his professional organization of my doctoral research. Having endless amount of research ideas, he inspired me to deeply explore the field of studies. His energy, wise advices and willingness to help made my stay at KTH productive and highly enjoyable.

I would like to thank my co-supervisor, Prof. Lech Wosinski, for inspiring discussions and sharing his technical expertise. Prof. Ilya Sychugov for endless patience and motivating ideas. Dr. Tommy Haraldsson for participation in desperate experiments. Prof. Min Yan, Prof. Muhammet Toprak and Prof. Jan Linnros for a generous sharing of your knowledge and openness for discussions. Thanks to Dr. Sergei Dyakov for inspiring theoretical discussions.

Thanks to all my colleagues from KTH who made my stay here unforgettable: Nicolas, Milad, Reza, Carlos, Gleb, Tomas, Ruslan, Xu, Federico, Jin, Xi. Special gratitude to Acreo team - Oskars, Xiaodan and Aleksejs: your hard-working and easy-going mood made my time in your lab full of good results. Thanks to colleagues from ICONE project: Giuseppe, Auro, Asif, Simone, Jaime, Aditya, Francesca, Ksenia, Tu, Marti, Faruk, Hugo, Hou-Man.

Finally, I would like to express my warmest acknowledgements to my wife and parents.

Спасибо за постоянную поддержку и любовь, дорогие мои. Спасибо маме с папой, брату и Нине, моему коальему дружку.

Aleksandrs Marinins
Stockholm, Sweden

List of Publications

Papers included in this thesis

A. **Aleksandrs Marinins,** Nicolas Knudde and Sergei Popov, "Air-suspended SU-8 strip waveguides with high refractive index contrast", Photonics Technology Letters, v. 34 (17), pp. 1862-1865, 2016.

B. **Aleksandrs Marinins,** Oskars Ozolins, Xiaodan Pang, Aleksejs Udalcovs, Jaime Rodrigo Navarro, Aditya Kakkar, Richard Schatz, Gunnar Jacobsen and Sergei Popov, "Thermal reflow engineered cylindrical polymer waveguides for optical interconnects", submitted to Photonics Technology Letters, 2017.

C. **Aleksandrs Marinins,** Oskars Ozolins, Xiaodan Pang, Aleksejs Udalcovs, Gunnar Jacobsen, Ilya Sychugov, Jan Linrros and Sergei Popov, "Free carrier absorption modulation in polymer waveguides doped with Si nanocrystals", manuscript prepared, 2017.

D. **Aleksandrs Marinins,** Zhenyu Yang, Hongzheng Chen, Jan Linnros, Jonathan G.C. Veinot, Sergei Popov and Ilya Sychugov, "Photostable Polymer/Si Nanocrystal Bulk Hybrids with Tunable Photoluminescence", ACS Photonics, v. 3 (9), pp. 1575-1580, 2016.

E. **Aleksandrs Marinins,** Reza Zandi Shafagh, Wouter van der Wijngaart, Tommy Haraldsson, Jan Linnros, Jonathan G. C. Veinot, Sergei Popov and Ilya Sychugov, "Light Converting Polymer/Si Nanocrystal Composites with Stable 60-70% Quantum Efficiency and Their Glass Laminates", ACS Applied Materials and Interfaces, v. 9 (36), pp. 30267–30272, 2017.

Conference presentations

F. **Aleksandrs Marinins,** Oskars Ozolins, Xiaodan Pang, Aleksejs Udalcovs, Jaime Rodrigo Navarro, Aditya Kakkar, Richard Schatz, Gunnar Jacobsen and Sergei Popov "Cylindrical Polymer Optical Waveguides with Polarization Independent Performance", Conference on Lasers and Electro-Optics (CLEO), San Jose, CA,14-19 May 2017.

G. **Aleksandrs Marinins**, Zhenyu Yang, Hongzheng Chen, Jan Linnros, Jonathan G. C. Veinot, Sergei Popov, Ilya Sychugov "Photostable PMMA/Si nanocrystal bulk nanocomposites with tunable emission spectra", Condensed Matter Division (CMD26), Groningen, Netherlands, 5-9 September 2016.

Related papers but not included in this thesis

H. Gleb Lobov, **Aleksandrs Marinins**, Sebastian Etcheverry, Yichen Zhao, Elena Vasileva, Abhilash Sugunan, Fredrik Laurell, Lars Thylen, Lech Wosinski, Mikael Östling, Muhammet Toprak and Sergei Popov, "Direct birefringence and transmission modulation via dynamic alignment of P3HT nanofibers in an

advanced opto-fluidic component", Optical Matererial Express, v. 7, pp. 52-61, 2017.

I. Gleb Lobov, **Aleksandrs Marinins**, Reza Zandi Shafagh, Yichen Zhao, Wouter van der Wijngaart, Lech Wosinski, Lars Thylen, Muhammet Toprak, Tommy Haraldsson, Mikael Östling and Sergei Popov, "Electro-optical effects of high aspect ratio P3HT nanofibers colloid in polymer micro-fluid cells", Optics Letters, v. 42(11), pp. 2157-2160, 2017.

J. Gleb Lobov, Y. Zhao, **Aleksandrs Marinins**, Min Yan, Jiantong Li, Abhilash Sugunan, Muhammet Toprak, Lars Thylen, Lech Wosinski, Mikael Östling and Sergei Popov, "Size impact of ordered P3HT nanofibers on optical anisotropy", Macromolecular Chemistry and Physics, v. 217, pp. 1089-1095, 2016.

K. Gleb Lobov, Yichen Zhao, **Aleksandrs Marinins**, Min Yan, Jiantong Li, Aghilash Sugunan, Lars Thylen, Lech Wosinski, Mikael Östling, Muhammet Toprak, Sergei Popov "Dynamic Manipulation of Optical Anisotropy of Suspended Poly-3-hexylthiophene Nanofibers", Advanced Optical Materials, v. 4, pp. 1651-1656.

L. Gleb Lobov, Yichen Zhao, **Aleksandrs Marinins**, Min Yan, Jiantong Li, Muhammet Toprak, Aghilash Sugunan, Lars Thylen, Lech Wosinski, Mikael Östling, Sergei Popov "Electric field induced optical anisotropy of P3HT nanofibers in a liquid solution", Optical Materials Express, v. 5(11), pp. 2642-2647, 2015.

M. Sergei Dyakov, Denis Zhigunov, **Aleksandrs Marinins**, Olga Shalygina, Polina Vabishchevich, Maksim Shcherbakov, Denis Presnov, Andrey Fedyanin, Pavel Kashkarov, Sergei Popov, Sergei Tikhodeev, Nikolai Gippius "Plasmon-polariton induced modification of silicon nanocrystals photoluminescence in presence of gold nanostripes", submitted to ACS Photonics, 2017.

N. Sergei Dyakov, Denis Zhigunov, **Aleksandrs Marinins**, M.R. Shcherbakov, Andrey Fedyanin, Alexandr Vorontsov, Pavel Kashkarov, Sergei Popov, Min Qiu, Margit Zacharias, Sergei Tikhodeev, Nikolai Gippius, "Optical properties of silicon nanocrystals covered by periodic array of gold nanowires", Physical Review B, v. 93(20), 205413, 2016.

Acronyms

CMOS	Complementary Metal Oxide Semiconductor
CPD	Critical Point Drying
CVD	Chemical Vapor Deposition
DUT	Device Under Test
EBL	Electron Beam Lithography
EBE	Electron Beam Evaporation
FCA	Free Carrier Absorption
FEM	Finite Element Method
FDTD	Finite-Difference Time-Domain
HSQ	Hydrogen Silsesquioxane
ICP-RIE	Inductively Coupled Plasma-Reactive Ion Etching
IR	Infrared
NCs	Nanocrystals
OEICs	Opto-Electronic Integrated Circuits
OSA	Optical Spectrum Analyzer
OSTE	Off-Stoichiometry Thiol-Ene
PDL	Polarization Dependent Loss
PECVD	Plasma Enhanced Chemical Vapor Deposition
PICs	Photonic Integrated Circuits
PL	Photoluminescence
QDs	Quantum Dots
QY	Quantum Yield
SEM	Scanning Electron Microscopy
SOI	Silicon-On-Insulator
TE	Transverse Electric
TM	Transverse Magnetic
TIR	Total Internal Reflection
WDM	Wavelength Division Multiplexing

Contents

Chapter 1

1 Introduction

1.1 Background

Since invention of a transistor, semiconductor industry brought us into the information technology era, where computers assist a majority of society's routines [1]. Growing computing and data exchange rates demanded more and more advanced technical solutions. Back in 70s, after the invention of laser, light was proposed as an incredibly efficient information carrier comparing to lossy copper interconnects [2]. With an appearance of low attenuation glass fibers and [3], later, erbium doped fiber amplifiers [4], optical communications took a major role in high capacity long distance data transmission, connecting the whole world. Optical communication wavelengths were chosen according to the lowest absorption in silica fibers, these transmission windows are centered at 1310 nm and 1550 nm [5]. Since its birth, optical communications experienced rapid technological growth up to combining with integrated electronics on the same chip. Nowadays, rapidly growing data traffic needs a large amount of fiber-optical components for efficient network functioning. Potentially, photonic integration can dramatically decrease system power consumption, overall equipment size and cost; while stability, flexibility and capacity will increase. In other words, substitution of bulk fiber-optics with photonic chips is highly beneficial [6].

To reduce PIC fabrication costs, capabilities of microelectronic semiconductor foundries are used. Silicon, which has been a leading material in microelectronic industry for decades, is an attracting platform for PICs thanks to transparency in the most widely used telecom wavelength bands, high refractive index contrast with cladding materials (SiO_2, polymers, air), well-known processing conditions and production scalability (up to 12 inch wafers) [7]. However, expensive silicon-on-insulator (SOI) wafers are needed to fabricate devices with moderate insertion losses. Less expensive polysilicon and amorphous hydrogenated silicon suffer from excessive losses, making these platforms far from real applications. III-V materials, compared to SOI platform, offer a unique opportunity to implement both active and passive devices on a single chip, but there are drawbacks such as near-infrared (IR) light absorption, high material costs and low fabrication yield due to poor mechanical properties [8, 9]. Several groups work on III-V material epitaxial growth on SOI platform attempting to combine advantages of both platforms, however, crystalline

lattice mismatch limits a quality of grown active layer [10].

This work is devoted to polymer photonics platform, which offers the best performance/cost ratio for many applications [11]. Optical polymers are less expensive than SOI and III-V material wafers, do not require epitaxial growth or chemical vapor deposition (CVD) techniques used for III-V and Si_3N_4. Some polymers can be directly patterned by lithography and wet development step avoiding use of expensive plasma etching tools [12]. Nanoimprint lithography is another cost-effective patterning technique thanks to softness and low melting point of most polymers. Propagation losses <0.07 dB/cm at 1550 nm reported for polymer devices [13]. This is close to silica-on-silicon waveguides, where are considered the lowest loss optical waveguides [14]. Another drawback of optical polymers is low refractive index, this leads to larger device size and limited integration density due to huge bending radii. On the other hand, this simplifies polymer optical chip packaging procedures. Low processing temperature of polymer photonics allows for back-end integration as a top layer of opto-electronic integrated circuits (OEICs). Up to date, Fraunhofer Heinrich Hertz Institute (HHI) in Berlin developed a state-of-the-art polymer photonics platform called PolyBoard [15]. Based on buried channel waveguides, it comprises a broad variety of photonic components such as multimode interference (MMI) splitters and couplers, thermo-optically tunable switches and variable optical attenuators (VOAs), arrayed waveguide gratings (AWGs) and many others. Low insertion loss polarization splitters/rotators are introduced by combining PolyBoard with thin film filter technology [16]. PolyBoard is successfully integrated with InP-based gain chips resulting in tunable distributed Bragg reflector (DBR) laser with wavelength span of 40 nm [17]. The Bragg wavelength of polymer waveguide grating is tuned thermo-optically without affecting gain section. Such polymer cavity approach results in highly stable single mode lasing. Finally, hybrid 40 channel 100 Gb/s transmitters for wavelength division multiplexed (WDM) networks were developed [18].

Another advantage of polymers is a possibility to combine it with graphene [19], to dope with semiconductor nanoparticles or organic chromophores for active applications like light emission, amplification or electro-optic modulation [20, 21]. This significantly broadens functionality of integrated photonic devices based on polymer platform. To this end, we investigated optical properties of polymers doped with Si nanocrystals (Si NCs). Bulk Si is a poor emitter due to indirect bandgap. Nanostructured silicon shows clearly different optical properties comparing with a bulk one [22]. When particle size goes below few nm, optoelectronic properties of Si NCs are governed by a quantum confinement effect [23]. This brings unique properties such as a quasi-direct bandgap, which greatly enhances light emissivity. One of the important parameters of Si quantum dot (QD) ensemble is quantum yield (QY). It determines the amount of optically active NCs in the whole ensemble. In glass matrices, it rarely exceeds 25%, while polymer matrices potentially offer higher QY. Inexpensive chemical synthesis of Si NCs in large quantities together with ease of polymer processing may result in a very bright photonics platform [24].

1.2 Research goals and achievements

Despite low fabrication complexity and high flexibility towards numerous applications, polymer platform needs to overcome several fundamental limitations to meet industry requirements. Considering trends and problems discussed in previous section, we set the following objectives for this work:

- to find and implement methods to enhance a performance of commonly used polymer waveguide-based passive devices: decrease propagation losses and polarization-dependent losses (PDL), shrink device size for denser integration;
- to integrate Si QDs into optical polymers yielding stable, efficient and low cost active optical materials for on-chip light modulation and emission.

Integrated polymer photonic components were proposed and fabricated using standard CMOS fabrication techniques. Developed devices include:

- air-suspended waveguides with high index contrast and low bending radii;
- cylindrical waveguides and microring resonators with low sensitivity to light polarization and decreased scattering losses;
- all-optical modulator based on polymer waveguide doped with Si NCs.

To broaden functionality of a polymer platform, Si NCs were encapsulated into different polymers and optical properties of resulting nanocomposites were evaluated over time. As an outcome, photostable hybrid materials with high quantum efficiency were obtained for the first time. Novel on-chip active photonic devices based on developed Si NC/polymer nanocomposites have been proposed.

1.3 Thesis outline

Chapter 2 briefly describes a theoretical background behind PICs and Si NCs. Light propagation in dielectric optical waveguide is explained by ray optic model and by solving Maxwell's equations. Different optical waveguide configurations discussed. Organic materials for optical applications are reviewed. Working principle of numerical simulation tools used to design integrated components is explained. Basic semiconductor physics of quantum confined Si NCs is given.

Chapter 3 introduces fabrication techniques and measurement methods used in this work. It covers clean room processes for polymer PIC fabrication, such as thin film deposition, lithography, plasma etching, etc. Chemical synthesis of Si NC/polymer hybrid materials described. Then, measurement setups for integrated component analysis and optical characterization of Si NC/polymer materials are presented.

Chapter 4 presents developed passive polymer components. Novel air-suspended SU-8 waveguides are evaluated in terms of propagation and bending loss, decreased bending radii reported. Thermal treatment method that decreases propagation losses and PDL in poly(methyl methacrylate) (PMMA) waveguides is discussed. Enhanced Q-factor of microring resonators after thermal treatment is demonstrated.

Chapter 5 describes a research on active optical materials based on Si NCs in polymers. Fabricated Si NC/PMMA and Si NC/OSTE nanocomposites show high QY values stable over many months. As an example of active applications, Si NC doped PMMA waveguides for all-optical intensity modulation are demonstrated.

Chapter 6 summarizes research results and proposes future work in the field.

Chapter 2

2 Theory and design of integrated photonic components

This chapter introduces a brief theoretical background of performed research. Operation principles of integrated photonic components are described. Semiconductor physics of Si quantum dots and their applications with polymer photonics are discussed. Numerical simulation methods for the design of micro-photonic components are presented.

2.1 Light propagation in optical waveguides

Theory. The main phenomenon responsible for the operation of optical fibers and PICs is called total internal reflection (TIR). It was first demonstrated by Daniel Colladon in 1841, his experiment showed a light confinement inside a parabolic stream of water (Figure 2.1a). TIR principle is schematically shown in Figure 2.1b, ray propagation model is a convenient way to demonstrate it. When light is incident on a boundary between transparent media with different refractive indices, there is a definite amount of transmitted and reflected light, depending on incidence angle. If a refractive index of the other boundary side is lower and incidence angle is greater than specific critical angle, there is no transmission and the ray is entirely reflected back to higher index medium.
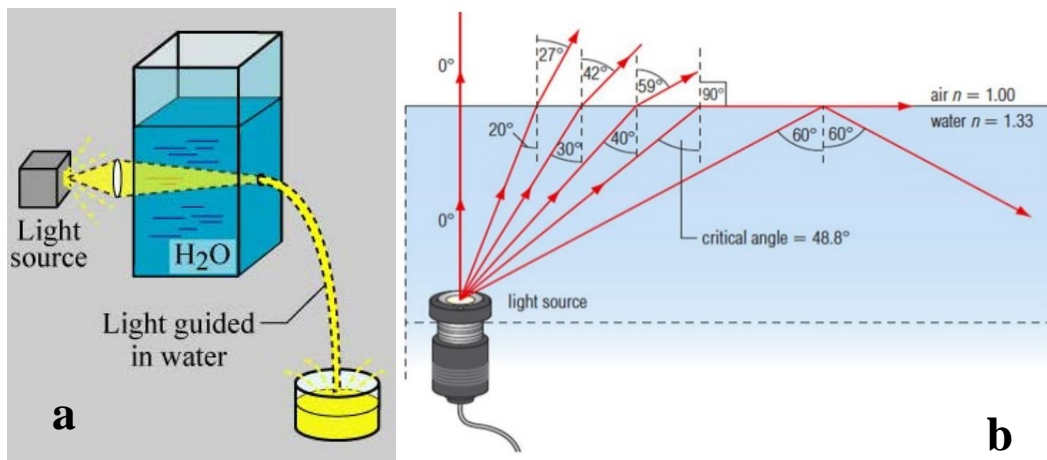

Figure 2.1 Colladon´s experimental setup (a) and TIR schematic representation (b).

According to Snell´s law, the critical angle, with respect to the normal to the interface, is dependent on a contrast between refractive indices:

$$\Theta_{crit} = \sin^{-1}\left(\frac{n_2}{n_1}\right) \quad (2.1)$$

where n_1 is a higher index material. Therefore, the light launched into a medium surrounded with lower refractive index media can be transmitted for long distances thanks to continuous reflections on boundaries [25]. In many cases it is assumed that these reflections generate a negligible phase shift. Such structure is called a waveguide since it confines light in one or two dimensions. A region with higher index is called a core and a surrounding lower index medium is called a cladding. One of the easiest examples is a glass rod in air. The most widespread application for TIR is optical fiber communications [2]. On-chip dielectric photonic circuit operation is based on the TIR phenomenon, like in optical fibers. This platform brings numerous data processing options in optical and electrical domains, compact size and scalable low cost fabrication. Depending on dimensions, refractive index contrast and wavelength integrated waveguides can guide multiple light paths or only a single one. Such discrete paths are called optical modes and waveguides can then support multimode or single mode light propagation [26]. For typical integrated polymer waveguides, core width and height are 2-3 μm, while standard single-mode fiber has a core diameter of 9 μm.

Ray optics model does not describe optical power distribution and relations between electric and magnetic field components, so electromagnetic wave model is more feasible for waveguide theory. As an electromagnetic wave, light propagating in waveguides can be expressed with Maxwell equations, where isotropic dielectric medium without free charges is assumed:

$$\nabla\times\mathbf{E} = -\frac{\partial}{\partial t}\boldsymbol{B} \quad (2.2)$$

$$\nabla\times\mathbf{H} = -\frac{\partial}{\partial t}\boldsymbol{D} \quad (2.3)$$

Here, $\mathbf{E}$ is an electric field, $\mathbf{H}$ is a magnetic field, $\mathbf{D}$ is an electric displacement field and $\mathbf{B}$ is a magnetic flux density. These vectorial quantities are related through $\mathbf{D} = \varepsilon\mathbf{E}$ and $\mathbf{B} = \mu\mathbf{H}$, where ε is a material permittivity and μ is a permeability.

For passive waveguides it is assumed that the permittivity is a spatial coordinate function and is constant in time. Using these assumptions with eq. 2.2, we obtain:

$$\nabla^2\mathbf{E} - \mu\varepsilon\frac{\partial^2}{\partial t^2}\mathbf{E} = -2\nabla(\nabla\ln(n)\cdot\mathbf{E}) \quad (2.4)$$

where n is a refractive index. The left part describes a wave equation while the right part deals with a spatial variation of a refractive index. For low core-cladding index contrast platforms the right side is assumed to be close to zero since gradient of refractive index is negligible.

Equation 2.4 can be further simplified by assuming the refractive index is constant and expressing $\mathbf{E}$ as $\mathbf{E}(\boldsymbol{r},t) = \mathbf{E}(\boldsymbol{r})e^{i\omega t}$, where $\boldsymbol{r}$ is a spatial coordinate vector and ω is an angular frequency. With that, a general solution can still be obtained for any region with constant refractive index, while boundary conditions can be assigned later. The

time dependency can also be extracted with an inverse Fourier transform. Equation 2.4 is then rewritten as the Helmholtz equation:

$$\nabla^2 \mathbf{E} + \mu\varepsilon\omega^2 \mathbf{E} = 0 \quad (2.5)$$

After substituting $\omega = \frac{2\pi c}{\lambda}$ and $\mu\varepsilon = \frac{n^2}{c^2}$, where c is a speed of light in vacuum and λ is a wavelength, we achieve:

$$\nabla^2 \mathbf{E} + \frac{4\pi^2 n^2}{\lambda^2} \mathbf{E} = 0 \quad (2.6)$$

Considering 3D waveguide with x and y coordinates representing a cross-section and light propagation along z axis, the Laplacian can be expressed as $\nabla^2 = \nabla_t^2 + \frac{\partial^2}{\partial z^2}$, where $\nabla_t^2 = \frac{\partial^2}{\partial x^2} + \frac{\partial^2}{\partial y^2}$. After applying this substitution to equation 2.6, we obtain:

$$\nabla_t^2 \mathbf{E} + k_0^2 n^2 \mathbf{E} = \beta^2 \mathbf{E} \quad (2.7)$$

Here, $k_0 = \frac{2\pi}{\lambda}$ is a vacuum wave vector magnitude and β is a propagation constant. β and k_0 define the effective refractive index of the particular mode through $n_{eff} = \frac{\beta}{k_0}$.

Analogic eigenvalue equation can be obtained for **H**. Computational techniques like finite element method, finite-difference time-domain, effective index method and others are typically used to solve such equations. As an outcome, one can obtain the effective index of any guided mode, and a mode field distribution profile.

Losses in waveguides. Propagation losses are the key parameter in waveguide operation. For dielectric waveguides, there are 3 main loss channels: scattering, radiation and absorption [27]. Scattering comes from waveguide surface roughness. It is easy to explain with ray model approach: when ray strikes a local interface roughness, the incidence angle there could be less than critical and part of the light goes to cladding. For a planar waveguide, interface scattering losses can be expressed with

$$\alpha_{scat} = \frac{\sigma^2 k_0^2}{\beta} \frac{E_S^2 \Delta n^2}{\int E^2 dx} \quad (2.8)$$

where σ is the surface roughness and $E_S^2 / \int E^2 dx$ is the normalized light intensity on core-cladding boundary [28]. Here, both surface roughness and index contrast are squared, showing a great influence on amount of scattering loss. This is usually the case with waveguides patterned by plasma etching due to sidewall damage done by ions [29].

Radiation losses arise from waveguide profile inhomogeneities, such as width variations and waveguide bending. To explain this, let's consider the mode entering a waveguide bending with curvature radius R. The tangential phase velocity of light must be proportional to bending radius to keep the phase front. As seen from Figure 2.2, at certain radius R + x_r the cladding tail must propagate faster than the mode

central part in order to preserve a phase front. This is not consistent, so the light beyond this radius leaks out of the waveguide. To find x_r, the following equalities are introduced, considering angular velocity ($\frac{d\theta}{dt}$) is the same for all waves:

$$R\frac{d\theta}{dt} = \frac{\omega}{\beta_0} \quad (2.9)$$

$$(R + x_r)\frac{d\theta}{dt} = \frac{\omega}{\beta_1} \quad (2.10)$$

where β_0 is the propagation constant of a core mode and β_1 is the propagation constant of a cladding mode. By combining 2.9 and 2.10, we obtain

$$x_r = R\frac{\beta_0 - \beta_1}{\beta_1} \quad (2.11)$$

Therefore, better light confinement with smaller evanescent tail provides smaller possible bending radii with moderate to negligible radiation losses.
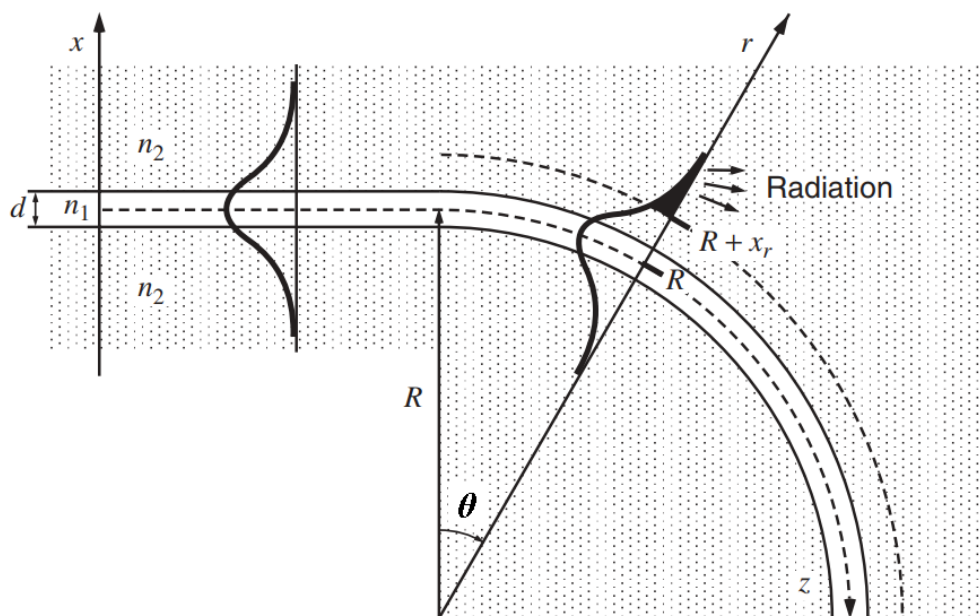

Figure 2.2 Schematic representation of radiation losses at waveguide bending [30].

In polymers, IR light is mostly absorbed by material-specific molecule vibration modes and their higher harmonics. We do not discuss electronic transition absorption here because it occurs at UV and shorter wavelengths. Molecule vibration absorption is induced mainly by hydrocarbon (C-H) groups and affects widely used optical communications windows [31]. Tailoring polymer chemical composition can dramatically reduce absorption; one of the approaches is to increase an effective mass of C-H oscillator. For example, substitution of H with F increases effective mass by a factor of 8, decreasing oscillator strength and associated absorption losses. Novel perfluorinated acrylate polymer waveguides demonstrate absorption losses smaller than 0.07 dB/cm [14], which is much lower than ones in InP where free carrier absorption is the main contributor [32].

Another crucial waveguide performance parameter is a polarization dependent loss (PDL). It is defined as loss varying when polarization state of propagating light

changes. In this work we deal with a difference between propagation losses of mode with transversely polarized electric field (TE) and transversely polarized magnetic field (TM). Normally, a signal from an optical fiber coupled to a chip has random polarization state, so polarization independent PIC performance is highly desirable, otherwise specific polarization management is required [33]. This is especially crucial for a proper operation of networks where polarization-division multiplexing is employed.

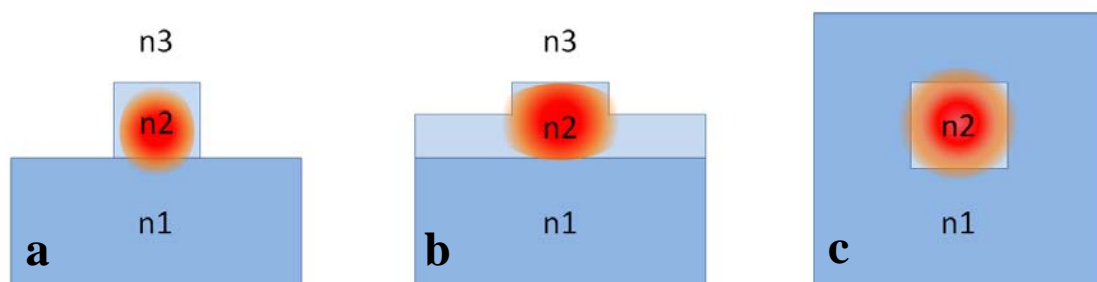**Waveguide types.** There are three major types of integrated polymer waveguide geometry, see Figure 2.3.

Figure 2.3 Profile of a strip (or ridge) waveguide (a), rib waveguide (b) and buried channel waveguide; n3<n1<n2.

In strip waveguides, a core has relatively high refractive index contrast with air cladding. Therefore, these waveguides confine light well from top and sidewalls. High light confinement allows sharper bends and, consequently, denser photonic integration, but at a cost of surface roughness induced propagation losses and a birefringence that stems from different refractive indices of top and bottom cladding. Rib waveguides possess lower propagation losses thanks to lower mode overlap with sidewalls, but the confinement is weaker, so larger bending radii are needed to prevent radiation loss to side polymer film. PDL can be decreased to negligible values by tailoring rib waveguide geometry; however, this effect is wavelength dependent. Buried channel waveguides show excellent propagation losses limited mostly by material absorption, and also polarization dependency is nearly negligible through the whole C-band. But, as one can see, refractive index contrast is the smallest in this case, making devices based on such waveguides quite bulky. So, depending on application requirements, one can choose the most suitable waveguide design, for example, buried channel waveguides are perfect for straight optical interconnects between chips on a printed circuit board [34]. In this work we investigate alternative geometries of strip waveguides.

2.2 Optical polymers

Polymers are solid organic materials consisting of many monomers linked to each other in a repetitive manner. Typically, polymers are highly transparent in visible and NIR region. Their refractive index ranges from 1.3 to 1.7 which is close to one of

glasses. Low refractive index contrast between polymer core and cladding puts some limitation on the size of integrated polymer devices [31]. On the other hand, a desirable refractive index can be obtained by modifying a chemical composition of a polymer to meet application-specific requirements. Optical polymers possess several advantages that make them attractive for photonic integration. First, high quality thin films can be deposited with inexpensive spin-coating techniques routinely used in microelectronic industry. Desired film thickness is easily obtained by changing polymer solution viscosity and/or adjusting spin-coating speed. In this way, polymer films can be obtained within several minutes without any use of expensive deposition techniques such as physical vapor deposition (PVD), epitaxy, etc. Also, a broad variety of substrates are available bringing a possibility to fabricate polymer waveguides on flexible plastic sheets [35], to combine polymer waveguides with Si and InP photonics [36, 37]. Another advantage is a low amount of internal stresses in polymer films which results in negligible birefringence comparing to silica waveguides, for example [38]. So, polymer channel waveguides typically have polarization independent performance and close to zero stress-induced losses [39].

There are many photosensitive polymers available for rapid direct PIC definition with conventional photolithography techniques followed by development. Considering fast film deposition via spin-coating, the whole optical circuit fabrication cycle can take only 30 minutes. Also, mechanical properties of polymers allow utilizing unconventional patterning techniques such as nanoimprint lithography and injection molding [40]. These rapid PIC formation techniques are a good alternative to plasma etching pattern transfer in case if light-insensitive optical polymers are used (polyimides and polycarbonates, for example). Another valuable property is a high thermo-optical coefficient of most polymers. It is typically about one order of magnitude higher than one of silica. This property is broadly exploited in various polymer thermo-optically tunable devices: switches, add-drop filters, DBRs, etc [15].

As it was mentioned in the previous section, polymeric materials have notable molecule vibrational absorption of NIR light, particularly in telecommunication window. Electronic absorptions occur in UV and DUV region and do not significantly contribute to absorption loss at optical communication wavelengths. Vibrational absorptions arise from high spring constants of C-H bonds. Oscillatory strength of these bonds is decreased by substituting low mass H atom with higher mass atoms like F or Cl. This approach resulted in a broad variety of low attenuation fluorinated polymers suitable for optical signal transmission in plastic optical fibers (POFs) and polymer PICs [41, 42]. However, one must consider that fluorination leads to refractive index decrease. Another issue with optical polymers is a thermal stability. In a presence of oxygen, most polymers experience chemical composition change at elevated temperatures, which leads to increased absorption of visible and NIR light. This effect is called yellowing and occurs mainly due to hydride reactions [41]. Currently, yellowing is minimized in highly fluorinated polymers where unstable H atoms are substituted with stronger C-F bonds. Even more, increased hydrophobicity of fluorinated polymers prevents water absorption, making performance of such optical polymers nearly insensitive to humidity.

For optical waveguide preparation we used two commercially available polymers: PMMA and SU-8 [43, 44]. Table 2.1 describes their basic properties.

Table 2.1 Properties of PMMA and SU-8

Material	Refractive index	Tg (°C)	Absorption loss (dB/cm)	Patterning techniques
PMMA (acrylic plastic)	1.482 @ 1310 nm 1.480 @ 1550 nm	95 - 106	0.5 @ 1310 nm 1 @ 1550 nm	DUV, e-beam, RIE, NIL
SU-8 (epoxy resin)	1.580 @ 1310 nm 1.575 @ 1550 nm	> 300	0.45 @ 1310 1.1 @ 1550	UV, e-beam, RIE, NIL

PMMA is a positive tone photoresist with thermoplastic properties. In other words, it melts at elevated temperatures. The higher the molecular weight, the higher is the glass transition temperature, at which polymer viscosity starts to decrease. Typically, PMMA with a molecular weight of 950000 is used.

SU-8 is an epoxy resin negative photoresist developed by IBM. In contrast to PMMA, SU-8 is sensitive to UV light and can be patterned with low-cost lithography tools like contact lithography. SU-8 is a thermoset polymer; it doesn't melt when it is fully crosslinked. Therefore, it is well-suited for applications where resistance to high temperature is needed.

Another polymer used in this work is off-stoichiometry-thiol-ene (OSTE) polymer [45]. It was used to prepare bulk hybrid Si NC/OSTE material. This polymer is synthesized by crosslinking thiol and allyl monomers. Refractive index, mechanical properties and hydrophobicity of this polymer are broadly tuned by varying ratio of precursor monomers. Also, it is rapidly polymerized with low shrinkage in a presence of a photoinitiator and UV light.

2.3 Luminescent Si nanocrystals

Silicon is the most studied semiconductor material in microelectronic industry [46]. Comparing with bulk Si, nanostructured Si possess clearly different semiconductor properties. It was first documented by Canham in his work on visible photoluminescence from porous Si [22]. While bulk Si has indirect bandgap with 1.12 eV energy, Si NCs have increased bandgap and quasi-direct transitions (Figure 2.4) [47]. When a semiconductor absorbs the energy higher than bandgap, an electron from the valence band is excited to the conduction band. In direct bandgap materials, like GaAs, the lowest energy state of conduction band has the same k-space momentum with the highest energy state of valence band, so, the excited electron directly recombines with the hole producing a photon. In indirect bandgap materials, like bulk Si, minimum and maximum energy states have different momenta, so, a phonon is needed to perform a radiative recombination, which lowers a photon emission probability.
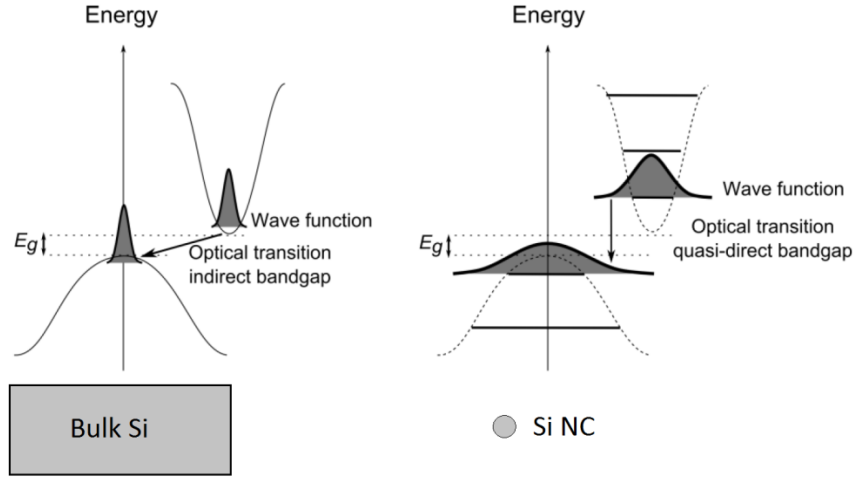
Figure 2.4 Band diagrams of a bulk Si and Si nanocrystal: carrier wave functions broaden and overlap.

In Si nanocrystals, a quantum confinement effect broadens carrier wave functions and increases the bandgap. This overlap allows more efficient radiative recombinations under UV-blue excitation. Increased bandgap results in higher energy photoluminescence ranging from NIR to blue, depending on a size of Si NC [48]. Quantum confinement effect emerges when at least one of the structure dimensions is close to Bohr radius of exciton (Coulomb force bound electron-hole pair):

$$a_b = \frac{\varepsilon \hbar^2}{\mu e^2} = \frac{\varepsilon m_0}{\mu} \quad (2.12)$$

where $\hbar$ is the Dirac constant, μ is a reduced mass, e is an electron charge and m_0 is a free electron rest mass. For Si Bohr radius of exciton is ~5 nm [49]. A comparison between energy bands of bulk material and spatially confined nanostructures is shown in Figure 2.5a. In the case with QDs, which are confined in three dimensions, carrier density of states turns into discrete atomic-like levels [50].
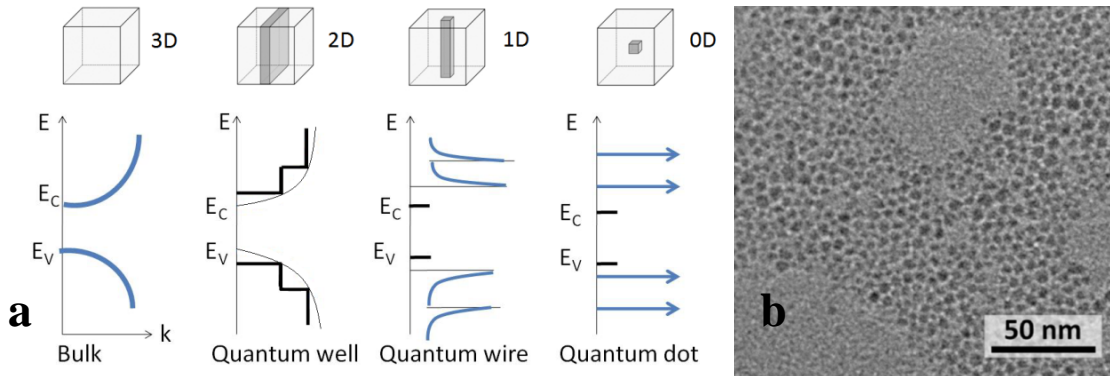

Figure 2.5 Density of states evolution upon transition from bulk material to a quantum well, confined in 1 dimension; to a quantum wire, confined in 2 dimensions; a quantum dot, confined in 3 dimensions (a); a TEM image of free-standing Si NCs (b).

QD carrier energy states can be obtained by solving the Schrödinger equation in a spherically symmetric potential using a particle in a box model:

$$E_{nl} = E_g + \frac{\hbar^2}{2\mu a^2} \chi_{nl}^2 \quad (2.13)$$

where a is a nanocrystal radius, χ_{nl} is the Bessel function, n is a principal quantum number, l is an orbital quantum number. From 2.13 it is clear that smaller QD radius leads to a stronger confinement, hence, the optical transition energy increases [51]. The quantum confinement effect also enhances oscillator strength in Si NCs, this provides a high 3rd order nonlinearity at least one order of magnitude higher than one of a bulk [52].
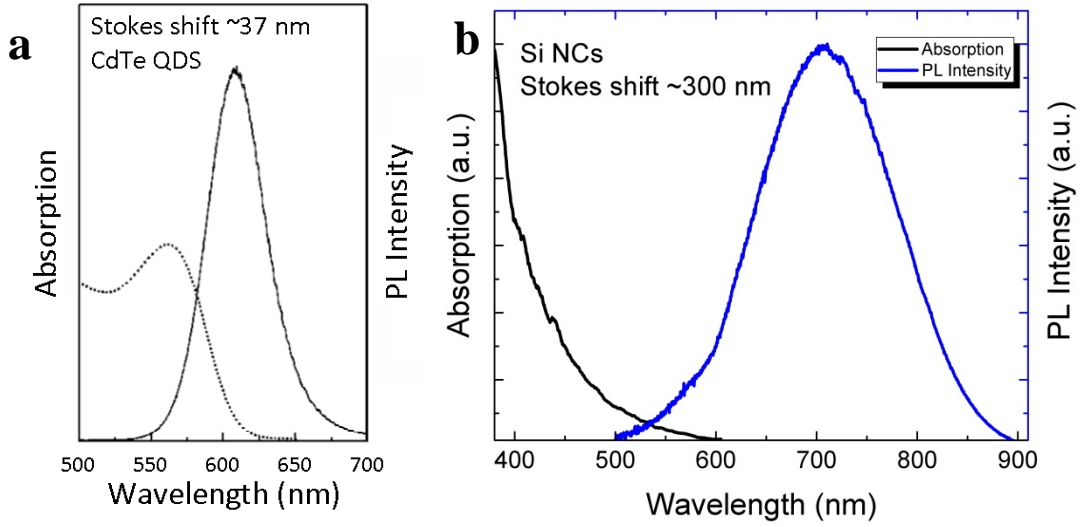

Figure 2.6 Stokes shift of direct bandgap QDs (a) vs one of Si QDs (b).

Another remarkable property of Si NCs is a large Stokes shift that comes from indirect bandgap structure of a bulk Si [53]. In comparison to direct bandgap materials, where absorption spectrum significantly overlaps luminescence spectrum, in Si NCs absorption states are distant from emission levels (Figure 2.6). Large Stokes shift prevents re-absorption of emitted photons by other NCs, which is a purely negative effect for photonic devices.

In this work, we assess quantum efficiency and photoluminescence lifetimes of prepared Si NC/polymer composites. We also characterize a stability of these parameters over time.

2.4 Numerical simulation tools

Theoretical investigations were conducted to achieve a desired device performance. Electromagnetic problem solvers were used to design PIC elements. Modern computational resources allow solving Maxwell's equations for complicated 3D photonic structures, where simple analytical approach does not provide a precise solution. Depending on a task, two frequently used methods were utilized: finite-

difference time domain (FDTD, OptiFDTD [54]) and finite element method (FEM, COMSOL Multiphysics [55]).

2.4.1 Finite element method

Normally, physical models are simplified into boundary value problems described by nonlinear partial differential equations, such as Maxwell's equations for electromagnetic problems, thermodynamics laws for heat transport, structural mechanics for stress evaluation, etc. This makes FEM a powerful tool for solving complicated practical problems with different physics involved [56]. For example, studies on electro-optical and thermo-optical devices, opto-mechanical system design. In this work, FEM is mostly used to solve optical modes. Practically, electromagnetic field distribution in optical waveguides plays a key role in an operation of photonic components such as directional couplers, waveguide bends, microring resonators, multimode interference devices (MMI), etc.

In 2D problems, the computational domain is divided into smaller triangular shape subdomains called finite elements. This approach has several advantages: an accurate discretization of complex geometry, simple representation of a global solution, detection of local effects (on a boundary between different materials, for example). Each subdomain is represented by a set of simple equations being a local approximation of complex partial differential equations. In each finite element, a local residual function is constructed to determine a solution convergence. All local functions are then assembled into global residual functions. Next, a solution can be numerically obtained by combining global residual functions with boundary conditions and initial values.

The simplified mathematical formalism behind a derivation of optical mode eigenvalue is described in chapter 2.1. Figure 2.7 demonstrates a graphical representation of calculated optical mode in an inverse rib waveguide.
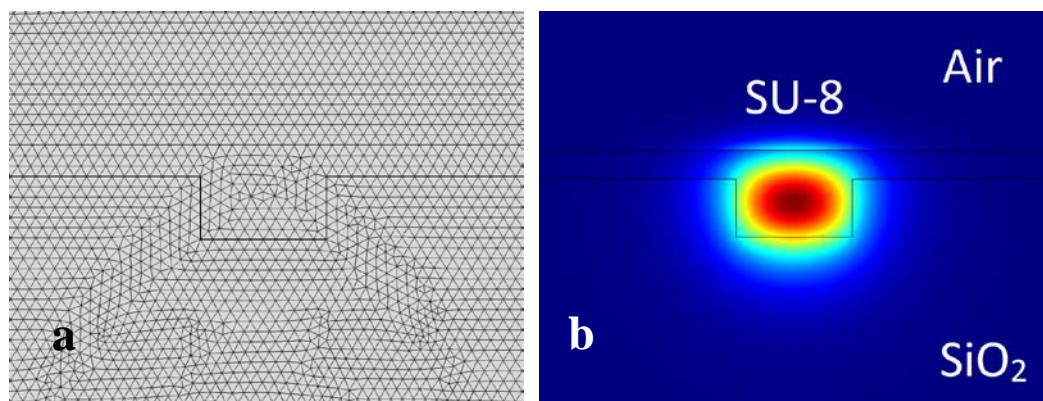

Figure 2.7 Inverse rib waveguide computational domain, meshed into subdomains (a) and computed electric field distribution at $\lambda = 1550$ nm (b), single mode light propagation confirmed.

2.4.2 Finite-difference time-domain method

FDTD method is used to solve Maxwell equations in time domain. The main idea is to divide the partial differential equations into spatial and time derivatives. The spatial equations are solved for a particular time node, then the next node is solved considering results from the previous time interval. Very accurate solutions can be obtained if enough simulation time is allocated together with high resolution in time and space. Also, being a time-domain method, FDTD solves problems for a range of wavelengths at a time, making it especially suitable for modeling PIC elements for WDM systems [57]. In this work, FDTD is used to simulate light propagation in photonic devices, such as a microring resonator (Figure 2.8) [58].

From this model, a free spectral range (FSR) between resonant wavelengths can be studied and a cavity quality factor (Q factor) can be estimated. Knowing the desired FSR, the resonator geometry is obtained through calculated waveguide group index:

$$n_g = n_{eff} - \lambda \frac{dn_{eff}}{d\lambda} \quad (2.14)$$

used in the following equation:

$$\Delta\lambda_{FSR} = \frac{\lambda^2}{n_g L} \quad (2.15)$$

where L is a microring length. Therefore, particular filtering properties can be achieved for further investigations. In a real device, the Q factor mainly comes from radiative, absorption and scattering losses in a cavity, FDTD can precisely calculate the first two. Absorption Q factor is obtained with:

$$Q_{abs} = \frac{n_g}{2n_{eff\,imag}} \quad (2.16)$$

where $n_{eff\,imag}$ is an extinction coefficient of a particular mode. A total Q factor, which is a sum of before mentioned loss sources, can be extracted through the following relation:

$$Q_{tot} = \frac{\lambda_0}{\Delta\lambda} \quad (2.17)$$

where λ_0 is a resonant wavelength and $\Delta\lambda$ is a full width of half maximum (FWHM) of a resonant peak.
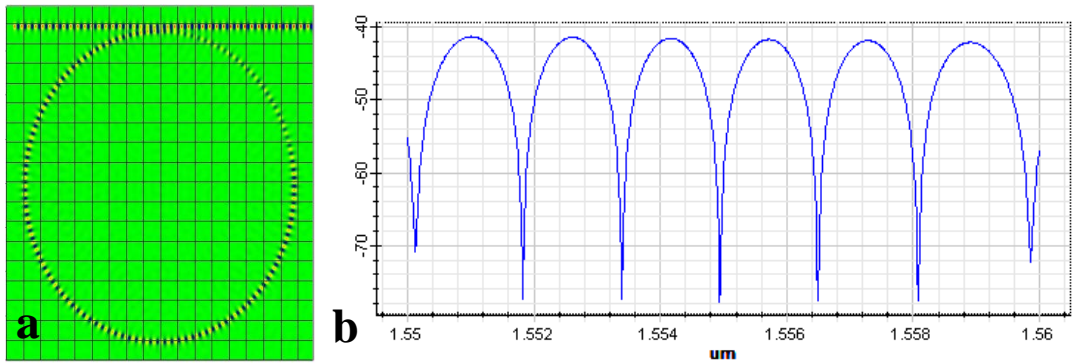

Figure 2.8 Simulated whispering gallery modes of a microring resonator (a) and it's transmission spectrum (b).

Chapter 3

3 Fabrication and Characterization methods

In this chapter, we introduce fabrication and characterization methods for both polymer PICs and polymer/Si NC materials. First, overview on integrated component and polymer material fabrication process is given. Physical principles of polymer thin film preparation, metal film deposition, lithography, wet and dry etching are described. Chemical synthesis of active polymers is briefly introduced. Then material and device characterization methods together with some experimental results are discussed.

3.1 Fabrication techniques

Fabrication procedures of polymer PICs are much simpler than modern CMOS chip processing. In principle, a lithography tool and a wet chemistry hood is enough to produce low complexity polymer PICs. Diagram below shows a simplified development flow from a bare substrate to a ready chip.
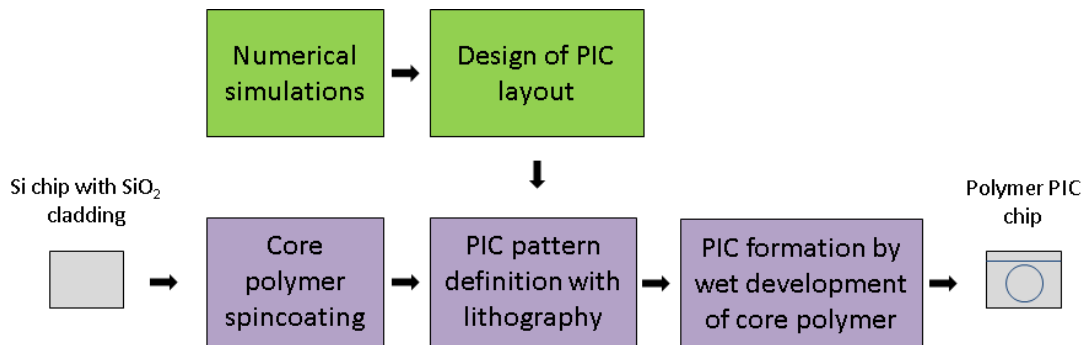
Figure 3.1 Polymer PIC development diagram

In research single chip fabrication is used, but this PIC development algorithm can be scaled up to 12 inch wafers for mass fabrication. First, core polymer layer is deposited via spin coating. Depending on PIC application, it can be a passive polymer or an active one; in this work active polymers were prepared by an addition of Si nanocrystals. Then a layout, derived from simulation results, is patterned on a core polymer by lithography (optical 405 nm contact lithography or electron beam lithography). After wet development PIC structures appear on a chip, this fabrication

method is called direct writing. In case if a core polymer cannot be patterned by direct writing, an imaging photoresist is spin coated on top of core polymer, exposed and developed, and then pattern is transferred to core by dry etching in plasma. Finally, chips are inspected with optical and scanning electron microscope (SEM), cleaved and sent to photonic probe station for optical characterization.

Fabrication of polymer components described in this Thesis was carried out in ELECTRUM cleanroom (Kista, Sweden) and in AlbaNova Nanofabrication facility (Stockholm, Sweden).

3.1.1 Polymer thin film preparation

Compared to SOI, Si_3N_4 and III-V platforms, polymer PICs are inexpensive thanks to extremely simple polymer thin film deposition technique called spin coating. It is an inherent process in semiconductor industry since photolithography was introduced in 1960s. The equipment ranges from low cost spinner with manual polymer solution feed to fully automatized station capable of processing tens of 12 inch wafers per hour. The coating mechanism is straightforward: after photoresist is dispensed on a center of a chip/wafer, a holder rotates with certain acceleration, speed and time regimes, providing centrifugal force which spreads a coating material into a uniform thin film. By adjusting spinning regime and choosing a polymer solution with definite viscosity, it is possible to deposit highly uniform films with thicknesses ranging from tens of nanometers to hundreds of microns. Figure 3.2 demonstrates typical spin coating curves for commercial Microchem PMMA photoresists [59].
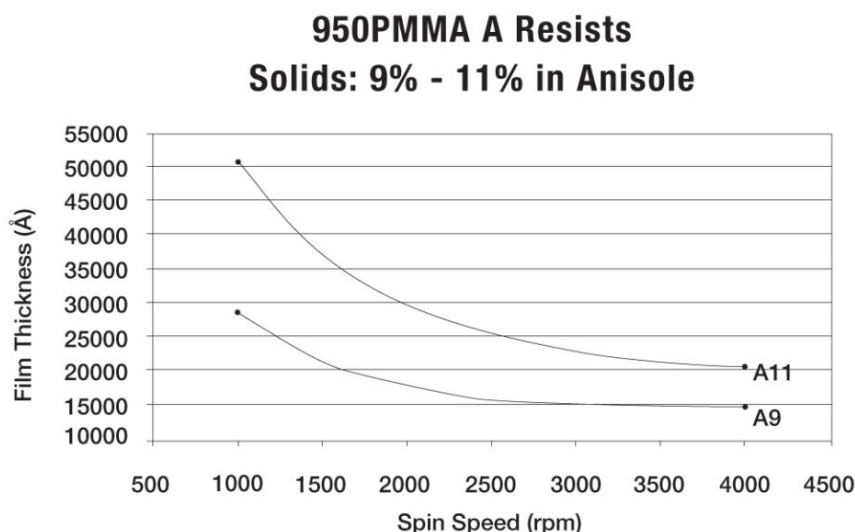

Figure 3.2 Coating thickness depending on spin speed for different viscosity resists.

If needed film thickness is out of available polymer solution viscosity, it is possible to dilute a solution to achieve smaller thickness or to perform multiple coatings to obtain thicker films. After polymer is spin coated, a substrate is soft baked on a levelled hotplate or in an oven. This is done to evaporate a solvent leaving solid thin

film. In some cases, solventless monomer solutions are used, then the film is solidified by baking together with UV curing until a polymer is cross-linked.

In this work, commercial photoresists Microchem PMMA A4 and A8, Microchem SU-8 2000.5 were used as passive waveguide core materials. For active components, PMMA powder from Sigma Aldrich was dissolved in toluene and mixed with Si NC-toluene colloid. After spin coating and soft bake, resulting solid thin films doped with Si NCs exhibited high optical quality.

3.1.2 Electron beam lithography

After polymer device layer is deposited by spin coating, a PIC layout is patterned with lithographic techniques. There is a broad variety of lithography methods, such as conventional optical lithography (436 nm g-line, 405 nm h-line, 365 nm i-line of mercury arc lamp), deep UV photolithography (248 nm KrF laser, 193 nm ArF laser), nanoimprint lithography (NIL) with quartz master, electron beam lithography (EBL), colloidal lithography, etc. In our experiments we used EBL for PICs with feature size below 1 μm and for custom photolithography mask writing. For the rest, contact h-line photolithography was used.

EBL is a lithography technique with the highest resolution among other lithography tools [60]. The main limitation of optical lithography, a diffraction limit, is beaten by using highly accelerated electrons. Their de Broglie wavelength is dramatically shorter than even 13.5 nm of extreme UV lithography. For example, at 25kV acceleration voltage electron de Broglie wavelength is around 7.6 pm. For EBL, the main resolution limitation is a resist material reaction to electron exposure.

EBL is based on the interaction of tightly focused scanning electron beam with resist material. Two types of reactions take place: molecule chain scission or cross-linking. In the first case, exposed area is soluble in a developer, leaving unexposed resist after development process. Such resists are called positive tone resists. PMMA is the most widely used low cost EBL resist. For negative resists, exposed area becomes cross-linked and insoluble in a developer, leaving exposed structures after development. SU-8 is an example of chemically amplified negative resist. The difference between positive and negative tone resists is schematically shown in Figure 3.3. After development and chip cleaving, directly-written microphotonic devices are ready for characterization.
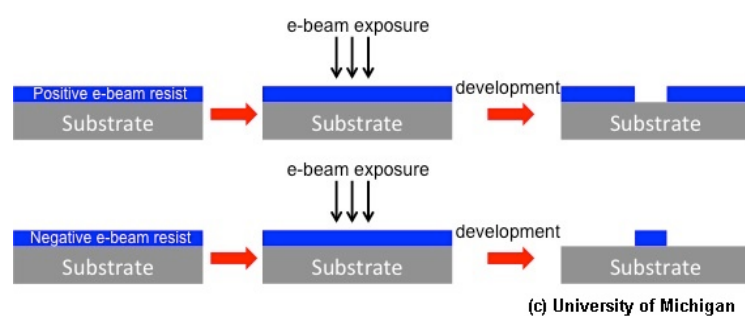

Figure 3.3 Exposure and development of positive and negative resists.

EBL system Raith 150 we used in Albanova Nanofab consists of the following main components: electron acceleration column, vacuum sample chamber with laser interferometer controlled precision moving stage, pattern generator computer and other electronic units. Figure 3.4 illustrates EBL system working principle.

Electrons emitted from a tungsten filament tip are accelerated by column voltage (25 kV max for Raith 150); electron beam is shaped with several coil-type magnetic lenses. Then a beam passes through an aperture which defines a beam size and a convergence angle. Smaller aperture provides higher resolution and higher depth of field at a cost of lower current, hence, longer exposure time. Next, deflecting lenses perform beam scanning according to a signal from pattern generator. A deflection angle limits writing fields (WF) to a maximum of 1x1 mm^2, so the whole pattern is divided into numerous WFs. After each field scan the stage moves to the next writing field.
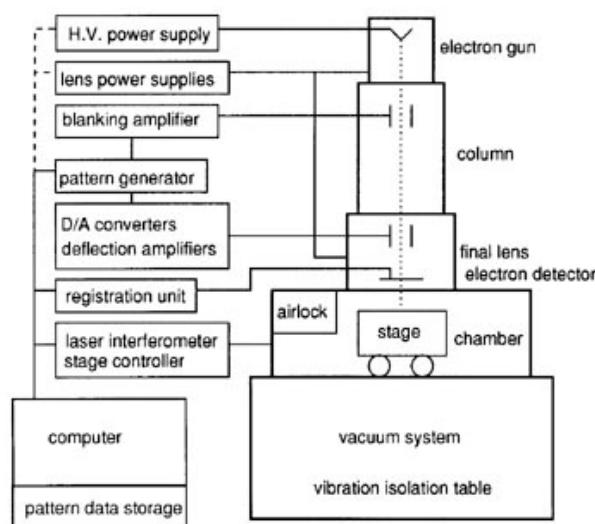

Figure 3.4 A scheme of the electron beam lithography system.

Another issue with EBL is a backscattering of electrons from resist/substrate interface. This is especially noticeable when exposing thick resists (2-3 microns). Backscattering can overexpose densely patterned structures due to broadening of exposure profile close to substrate interface. This problem is solved by use of smaller apertures for higher depth of field, higher acceleration and numerous dose tests. The amount of backscattering is also dependent on substrate material, for example, in our experiments it was determined that much less scattering occurs on polymer/polymer interface, rather than silica/polymer one.

3.1.3 Optical lithography

Despite excellent resolution and maskless patterning, EBL is a research tool and cost wise is much less beneficial than standard UV contact lithography. We used Karl Suss MJB3 mask aligner (405 nm h-line) and a home-made UV LED (390 – 400 nm)

compact lithography tool (Figure 3.5a). As with EBL resists, photoresists divide into positive and negative tone. To expose a photoresist, a sample is brought to a tight contact with Cr mask with some help of vacuum or mechanical clamps. Then a sample is irradiated with homogeneous collimated UV light (Figure 3.5b). Contact lithography does not need any expensive projection optics like in steppers, but has a limited resolution (~1 μm) and a reduced operation time due to mechanical contact with samples [61]. For low index contrast polymer PIC fabrication this resolution is fairly enough. Even more, in this work we demonstrate a method to decrease some feature size slightly below 400 nm. SU-8 resist devices can be directly written, while PMMA is not sensitive to ~400 nm light. So, it was patterned by first exposing UV-sensitive photoresist (Microposit S1818) on top of it and then dry etching PMMA layer.
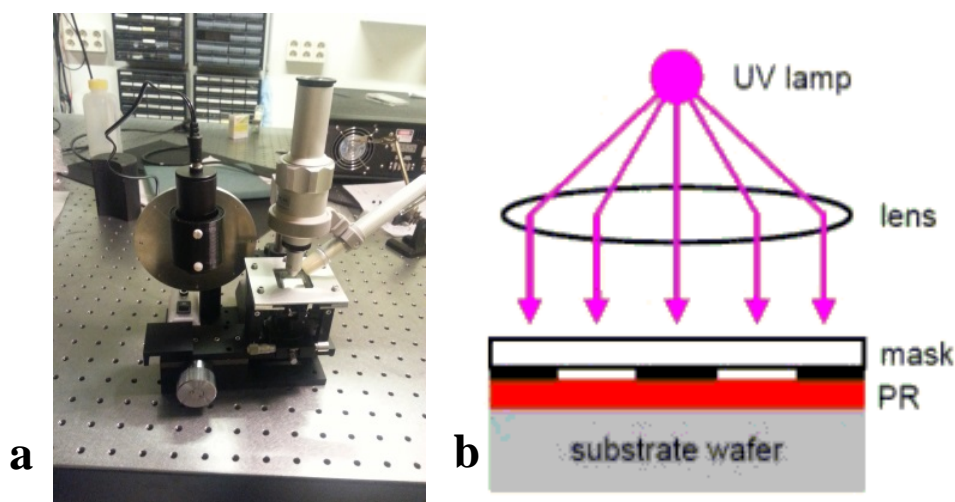

Figure 3.5 Home-made UV LED lithography tool (a) and contact lithography exposure scheme (b).

3.1.4 Metal film deposition

In our fabrication and characterization procedures, we used electron beam evaporation (EBE) technique to deposit metal films. We coated glass slides with chromium layer to fabricate custom photolithography masks and evaporated gold on polymer samples to provide a good conductivity for scanning electron microscopy (SEM) imaging. EBE is a physical vacuum deposition method based on heating and subsequent evaporation of a material to deposit [62]. Figure 3.6 shows a simple drawing of Eurovac EBE system used in AlbaNova Nanofabrication facility.

Electron gun, consisting of a heated filament, emits thermal electrons which are deflected and focused on a crucible with a magnet. Electron bombardment heats a material in a crucible to fume formation temperatures. Gold is first melted and then evaporated with increasing electron gun current; chromium is evaporated directly from solid state, this phenomenon is called sublimation. Evaporated atoms fly towards a sample and condense there due to thermal energy loss in a contact with a room

temperature substrate. Very low pressure (around 10^{-7} mbar) should be kept to obtain high purity uniform films. A deposition rate is dynamically monitored by quartz crystal sensor. Typical deposition rates for Au and Cr are 1-2 Å/s. It is worth noting that some procedures with photoresists are not compatible with EBE due to x-rays which emerge when energetic electrons bombard a material in a crucible. These x-rays easily expose photoresists.
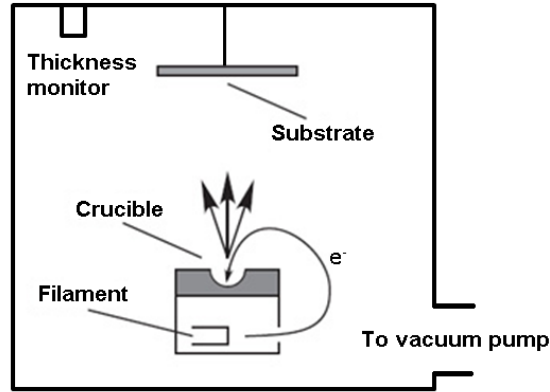

Figure 3.6 Electron beam evaporation vacuum chamber scheme

3.1.5 Reactive ion etching

In our fabrication we also used reactive ion etching (RIE) to pattern PMMA, SiO_2 and Cr. By optimizing recipes, it is possible to achieve high etch anisotropy, hence, vertical sidewalls of patterned devices. We used Oxford Plasmalab 100 machine at AlbaNova Nanofab, Figure 3.7 illustrates a chamber sketch and a work principle [63].
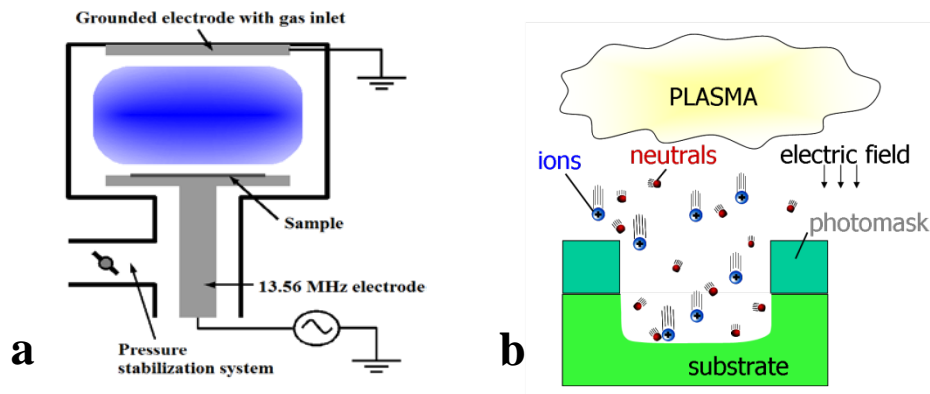

Figure 3.7 RIE chamber scheme (a) and sample etching principle (b).

The system consists of the following main parts: a vacuum chamber with precise gas flow control, capacitive electrodes with RF generator to ignite and sustain plasma, a sample holder with temperature control unit, and others. A RIE mechanism is divided into 2 components: chemical etching and physical sputtering. Let´s take SiO_2 etching as an example [64]. CHF_3 gas is added to a chamber to generate plasma with

CF_x radicals between parallel plate electrodes. The higher RF power, the higher is a density of reactive radicals. Plasma ions are accelerated by electric field and bombard a sample surface. CF_x radicals react with SiO_2 producing gaseous SiF_4, CO and CO_2. Also, carbon-fluorine polymers are deposited in etch area. Other accelerated ions physically sputter these polymers from surface, however, polymers on sidewalls stay untouched and block chemical etching in horizontal direction. So, high anisotropy can be achieved.

There are many parameters influencing etch performance: RF power, chamber pressure, gas flow and composition, temperature. Higher RF power means higher etch rate, but higher sidewall roughness is generated. Lower pressure lowers ion collision probability, thus, anisotropy is higher, but etch rate is lower. Addition of inert gases like Ar adds more physical sputtering. Table 4.1 shows recipes for low roughness, vertical sidewall etching of PMMA, SiO_2 and Cr.

Table 3.1 Optimized RIE recipes

Materials	PMMA	SiO_2	Cr
O_2 flow	10 sccm	-	8 sccm
CHF_3 flow	-	10 sccm	-
Cl_2 flow	-	-	2 sccm
RF power	100 W	150 W	20 W
Pressure	10 mTorr	5 mTorr	20 mTorr
Etch rate	~200 nm/min	~25 nm/min	~4 nm/min

3.1.6 Wet etching

Wet etching was performed to suspend microphotonic devices in air and to modify SiO_2 cladding under devices. Compared to dry etch in plasma, wet etching is a clearly chemical process which needs only glassware and a heater. In case with SiO_2, wet etching in buffered hydrofluoric acid (BHF) is an isotropic process (Figure 3.8).
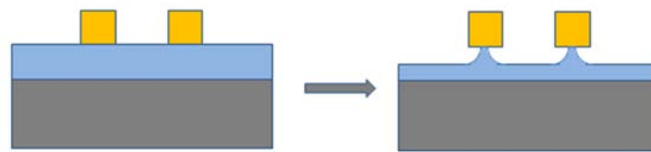

Figure 3.8 Isotropic underetch of SiO_2 cladding under optical waveguides.

BHF is a 49% hydrofluoric acid (HF) diluted with 40% ammonium fluoride (NH_4F) in 1:7 ratio. Comparing with undiluted HF, BHF is less reactive and does not peel off a photoresist, etch rate is about 100 nm/min at room temperature (~1500 nm/min for 49% HF), so better control can be achieved [65].

In case of complete etch of SiO_2 layer under photonic devices, specific drying need to be applied, otherwise capillary forces break waveguides. Then critical point drying technique is applied, it provides liquid to gas transition via critical point. There, densities of a liquid phase and gas phase are equal. At this condition, capillary forces

are negligible and devices are dried safely. Liquid CO_2 is a mostly used drying agent due to its low critical point temperature (304.25 K at 7.39 MPa) [66].

3.1.7 Polymer/Si nanocrystal hybrid material preparation

Hybrid polymer/Si NC materials for active components were prepared by well-known polymerization reactions with addition of photoluminescent Si NCs colloid. As host matrices, poly(methyl-methacrylate) (PMMA) and off-stoichiometry thiol-ene (OSTE) polymer were used [45, 67]. PMMA is synthesized from mono(methyl-methacrylate) (MMA) monomers; OSTE is synthesized from thiol monomers and allyl monomers, which exhibit so called click-chemistry reaction. In order to start polymerization reaction, initiator is added and activated thermally or optically (UV-curing). Both polymers exhibit high transparency in visible and near-IR and high stability. Figure 3.9 shows active polymer synthesis scheme.
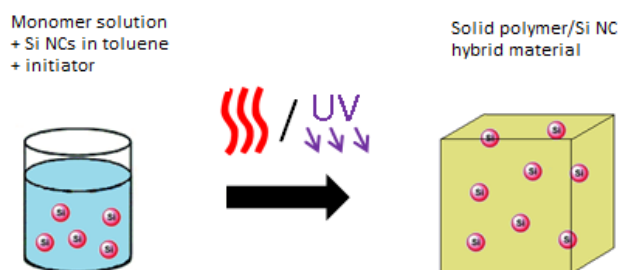

Figure 3.9 Polymer/Si NC hybrid preparation: from liquid to solid.

Synthesis does not require vacuum equipment and other expensive tools. Monomer solution is poured into reaction vial, polymerization reaction initiator is added (Azobisisobutyronitrile for PMMA and Irgacure 184 for OSTE), Si NCs dispersed in toluene are added and the mixture is properly stirred until all components are homogeneously distributed. We used Si NCs with alkyl and hydride surface passivation chemistry in our experiments. Next, thermal or UV light treatment triggers active radical formation from initiators. The role of active radicals is to drive polymerization reaction in parallel with a passivation of missing bonds on Si NCs, making them optically active and, thus, increasing quantum efficiency. As a result, transparent polymer material with light emitting Si NCs is synthesized. With this approach, several cm^3 of active material are fabricated per batch. Characterization includes an assessment of absolute photoluminescence quantum yield (QY) and free carrier lifetimes over time, to ensure prepared hybrids are optically stable.

3.2 Characterization methods

This part briefly explains material and device characterization techniques. Material characterization covers optical properties of photoluminescent polymer/Si NC hybrids. The quality of device fabrication processes is evaluated with a microscope inspection. Then waveguide performance is assessed with transmission experiments.

3.2.1 Material characterization

To investigate quantum efficiency and carrier dynamics of Si NCs in polymers, two measurement setups were used.

(1) In the first setup employing integrating sphere (Figure 3.10) absolute QY and photoluminescence (PL) spectra were obtained. Absolute QY is a ratio of absorbed and emitted photons, it describes light conversion efficiency of a material under study.
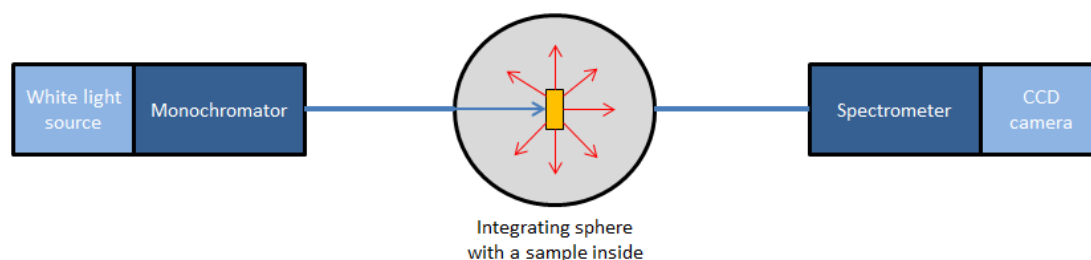

Figure 3.10 QY measurement setup with integrating sphere.

Light from a laser driven white light source (Energetiq EQ-99) is directed to a monochromator (SP2150i, Princeton Instruments) which selects a narrow (~5 nm) band for a sample excitation. Monochrome light is then coupled to an optical fiber with core diameter of 1 mm and guided to an integration sphere (Labsphere) with a sample inside. In the integration sphere, excitation light is spatially uniformly distributed due to diffusive scattering, providing uniform excitation of a sample excluding any directionality effects [68]. PL and excitation signals are then entering a fiber-coupled output port which is connected to a spectrometer with a thermoelectrically cooled CCD camera (PIXIS 100B, Princeton Instruments). Absorbed and emitted power is measured and recalculated to a photon number considering excitation and emission spectra photon energy. Then absorbed/emitted photon ratio, the QY, is calculated. Spectra are corrected with sensitivity curves obtained by recording CCD response to the same white light source. Reference samples with the same matrix but without Si NCs were measured; their spectra were subtracted from polymer/Si NC spectra to separate Si NC signal from matrix response.

(2) PL lifetimes were studied with another setup schematically shown in Figure 3.11. 405 nm laser diode (Omicron PhoxX) in pulsed mode is used as a pump source, it excites a sample under ~20° incidence. This configuration, called dark field, has a smaller amount of excitation light scattered into microscope objective, comparing to bright field where both excitation and collection have the same optical path. A notch filter after laser provides monochromatic excitation. PL signal is collected with objectives (Zeiss, 10x 0.25 NA, 100x 0.7 NA) and sent to an avalanche photodiode (APD) or to a spectrograph (Andor-Shamrock 500i) with thermoelectrically cooled electron-multiplying CCD camera (Andor-iXon3-888).
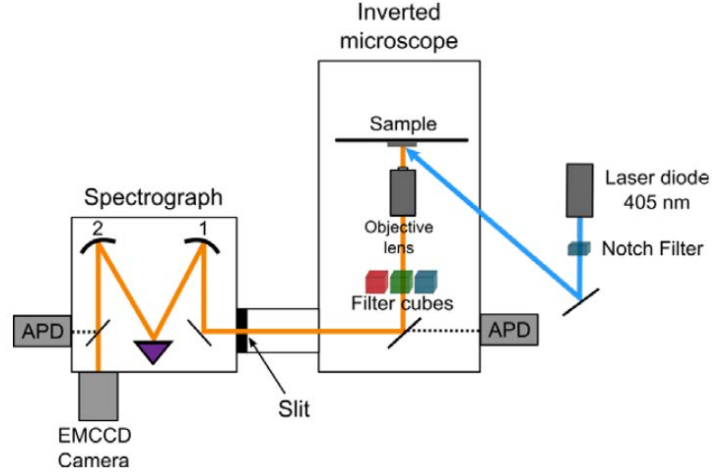
Figure 3.11 Micro-PL setup for spectrum and carrier lifetime measurements (1 and 2 are concave mirrors).

So, this setup also allows for PL imaging and spectrum measurements by using a mirror or a dispersive grating, respectively.

The PL lifetime is a time period when excited carriers recombine through radiative and non-radiative transitions to $1/e$ times initial excited carrier amount after excitation is stopped [69]. Considering approximate Si NC PL lifetimes are in the tens of μs range, which comes from indirect band gap nature of bulk Si, pump source pulse width and a period are adjusted to catch PL build-up to a steady-state and decay after excitation pulse is turned off. Typical time-dependent PL signal is shown in Figure 3.12.
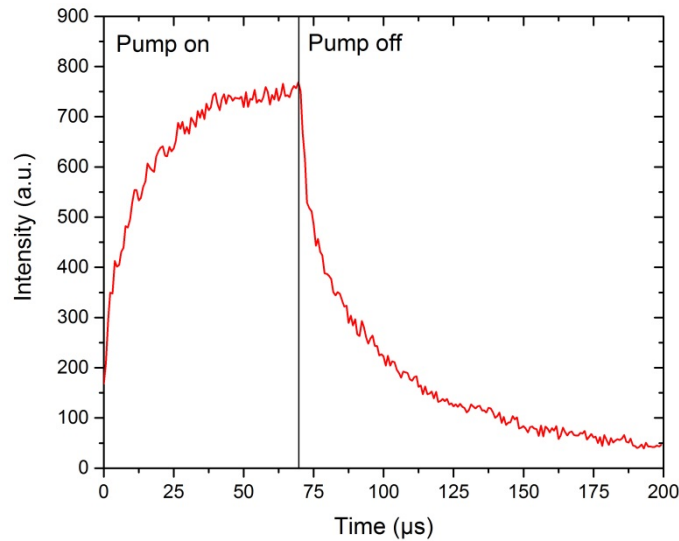

Figure 3.12 Build-up of PL signal and decay after pump is switched off.

In our samples, ensembles of different size Si NCs were studied, so the decay curve represents a set of individual decays with high dispersion (5 – 45 μs reported, smaller NCs recombine faster). This curve can be described with a stretched exponential function:

$$I(t) = I(0) * \exp(-(t/\tau)^\beta) \quad (3.1)$$

where β is a dispersion factor, which is typically around 0.8 – 0.9 for samples with internal QY near unity (either "dark" or "bright" Si NCs) [70]. Also, spectrally-resolved PL decay time measurements can be done by filtering PL and detecting only narrow spectrum part. In other words, measuring decay time of same size Si NCs. With absence of blinking NCs, numerically corrected spectrally-resolved ensemble lifetime measurements show mono-exponential decay curves, similar to single dot PL decay.

3.2.2 Device characterization

(1) To analyze sample surface topography, optical microscope and stylus profilometer are frequently used. Optical microscopy allows for brief assessment of fabricated PICs; single waveguide width of 2-3 microns makes it easily resolved with optical methods. Stylus profilometer (KLA-Tencor P-15) is a fast and easy-to-operate alternative to atomic force microscopy (AFM) where feature size exceeds ~1.5 μm. This limitation is primarily due to stylus tip size. Profilometer allows precise height and surface roughness measurements.

Another technique for more detailed topography analysis is a scanning electron microscopy (SEM, Fei Nova 200). It is similar to EBL; SEM imaging is based on a detection of scattered electrons when accelerated electron beam scans a sample surface. Detection of secondary electrons emitted as a result of inelastic scattering brings topography information, while back-scattered electrons from elastic scattering are used for sample composition analysis. In our experiments, polymer chips were coated with thin gold layer and grounded to avoid charging effects.

(2) For the measurements of integrated component waveguiding properties butt-coupling photonic probe station was assembled (Figure 3.13). It consists of a sample holder on XYZ micro positioning stage, lensed or tapered fibers fixed on XYZ micro positioning stages to couple/collect light from components, alignment microscope, sample illumination, tunable diode laser (Agilent 8164A) with polarization controller, optical spectrum analyzer (OSA, Agilent 86082A). Depending on experiment design, other tools were also used. Butt-coupling method allows broadband and polarization insensitive operation, however, is quite sensitive to misalignment. We used lensed fibers with focal spot diameter of 2±0.5 μm and focal distance of 5±1 μm from Nanonics [71]. Tapered fibers with tip diameters of ~500 nm were fabricated by immersing well-cleaved fiber tips in hydrofluoric acid. As a part of photonic probe station, fibers are fixed and carefully positioned with XYZ micrometer stages to obtain the lowest possible coupling losses (Figure 3.13). To control a polarization of light entering waveguides, light from fixed coupling fiber was sent to free space polarimeter (PAX IR-3, Thorlabs) and adjusted to TE or TM polarization with Babinet-Soleil compensator-based polarization controller.
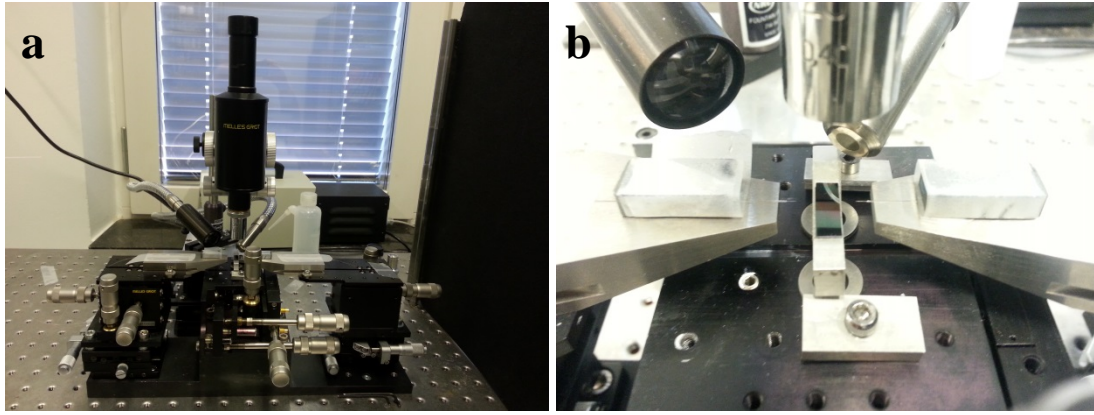
Figure 3.13 Experimental photonic probe station (a) and a closer view of a sample holder with incoupling and outcoupling fibers (b).

Before launching IR light, all alignment operations are done with visible 632 nm fiber-coupled laser to simplify the process. The following component parameters were measured with a discussed setup: insertion losses, waveguide propagation losses, polarization dependent losses (PDL), waveguide bend losses, wavelength-dependent transmission. Also, high speed modulated signal was transmitted to evaluate waveguide performance as an optical interconnect. Figure 3.14 illustrates a typical experiment performed with photonic probe station.
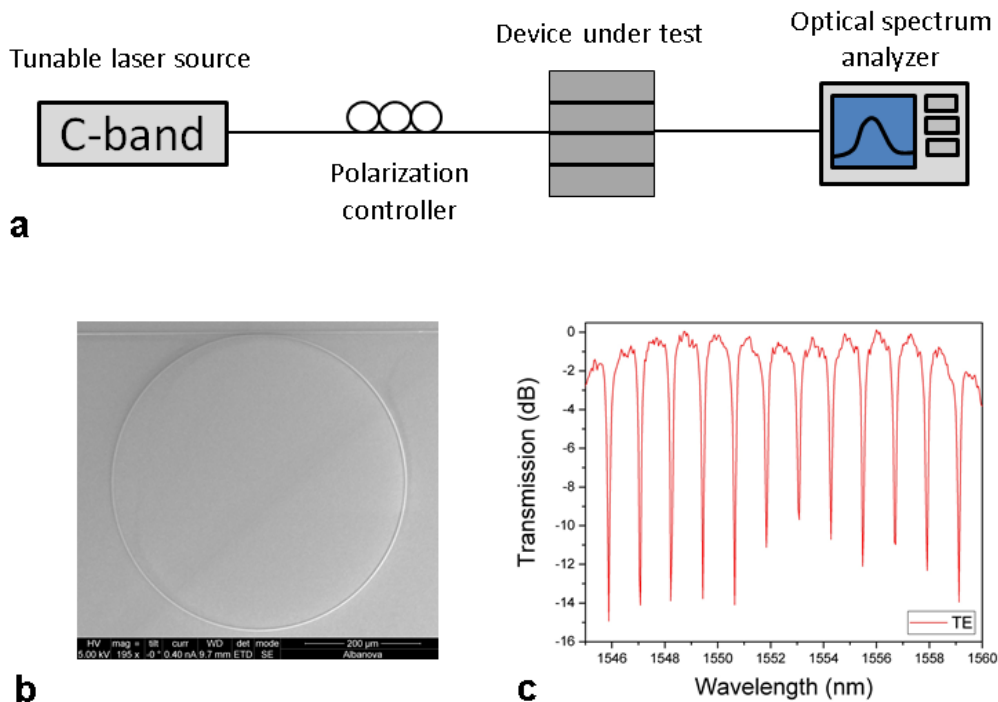

Figure 3.14 Characterization of microring resonator: experimental setup scheme (a), SEM image of microring under test (b) and its transmission spectrum (c).

Chapter 4

4 Passive integrated polymer components

In this chapter passive polymer waveguide-based microphotonic devices are presented. We focus on waveguides as they are a major group of optical devices in PICs; also, components like microring resonators, splitters/couplers, interferometers and others are based on waveguides. So, enhancement of waveguide performance leads to efficiency increase of almost every component in a PIC. This chapter is structured as follows. Section 4.1 demonstrates air-suspended SU-8 epoxy waveguides with a strong light confinement and low bending radii **(Paper A).** Section 4.2 shows thermally reflown circular core profile PMMA waveguides with low birefringence and propagation losses; microring resonators based on these waveguides are also evaluated **(Paper B).**

4.1 Air-suspended SU-8 waveguides

The major drawback of low refractive index systems is a poor light confinement which leads to a large device footprint [72]. This is especially notable with polymer waveguide bends where >100 μm radii are needed to prevent radiation losses and leakage to a substrate [73]. This limitation affects integration density and PIC design freedom which is a challenge even with low bending radii like in SOI platform. We propose stronger and more uniform light confinement by removing oxide cladding underneath polymer waveguides. In this way, we obtain kind of a channel waveguide surrounded by air cladding with a refractive index contrast reaching 57.5% (n_{SU-8}=1.575 vs n_{air}=1 at λ=1550 nm). To compare, it is only 0.4% for standard single mode optical fiber designed for 1550 nm wavelength. Obtained 57.5% contrast allows a development of more miniature polymer waveguides with small bending radii. SU-8 polymer was chosen because of its high refractive index, good mechanical properties and chemical inertness against acids used in fabrication [74]. Similar approach has already been implemented with SiO_2, Si, InP and polymer waveguides, however, supporting side anchors did not allow sufficiently dense integration [75]. We designed free-standing strip waveguides with small supporting nanopillars underneath (Figure 4.1a, b). These nanopillars are not affecting waveguide lateral dimensions and are small enough to prevent substrate leakage. It was determined experimentally that waveguides are mechanically stable if a distance between pillars is less than 50 μm.
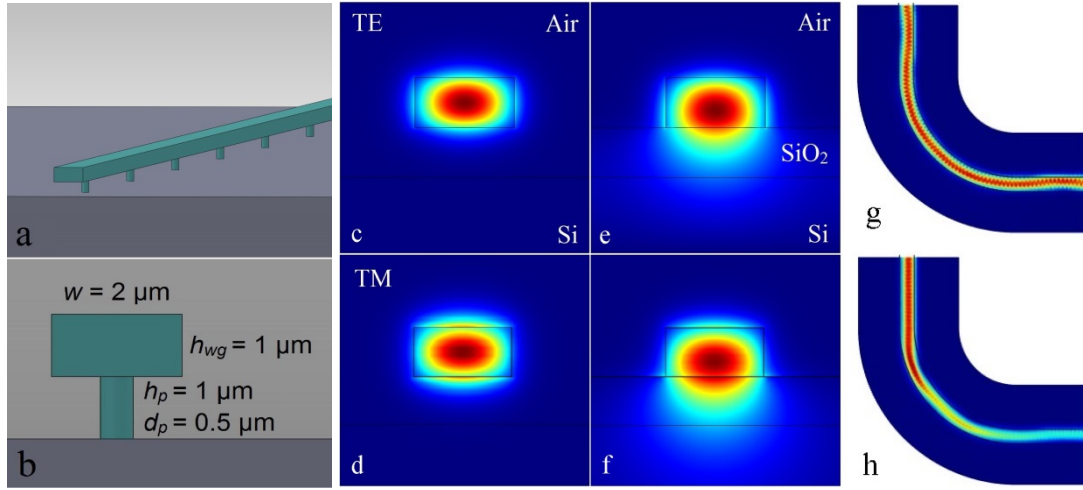
Figure 4.1 Schematic view of a suspended waveguide (a) and profile dimensions (b); field distribution in suspended (c, d) and non-suspended waveguides (e, f); simulations of 15 μm radius bend loss in suspended (g) and non-suspended waveguide (h).

Proposed waveguides were theoretically studied with FEM using COMSOL Multiphysics software. 2D simulations were employed for mode analysis considering that single mode behavior is highly important for correct component operation. Different core profiles were investigated from square to horizontal rectangular; we decided to fabricate a rectangular one to demonstrate a dramatic enhancement of light confinement in vertical direction, especially for TM mode (Figure 4.1c, d, e, f). As substrates, we had Si wafers with 1 μm of thermally grown SiO_2 layer. In case with waveguides sitting on SiO_2 cladding simulations show large substrate leakage, however, sweeping cladding thickness up to 20 μm revealed nearly the same result. This points on a waveguide profile as a main reason of light leakage. As estimated, removal of SiO_2 cladding results in much better light confinement and proper isolation from a substrate. 3D simulations were run to study bending radii dependent losses (Figure 4.1g, h). As expected, suspended waveguides greatly outperform non-suspended ones; already at 15 μm radius suspended waveguides possess ~0.15 dB loss per 90° bend, while non-suspended waveguides lose ~6 dB of optical power making such bending impractical for applications.

The fabrication route included 2 lithography steps, 1 plasma etch and 1 wet etch with critical point drying (Figure 4.2a). In short, supporting nanopillar pattern is first created with EBL in 1 μm thick PMMA resist mask spin coated on oxidized Si substrate. It is worth noting that instead of EBL less expensive lithography tools like conventional mercury lamp steppers are capable of fabricating proposed waveguides making them more cost-effective. Then nanopillar pattern was transferred to SiO_2 layer by dry etching it in CHF_3 plasma. Created holes in SiO_2 act as templates for nanopillars. Next, SU-8 core layer is spin coated in 2 rounds (500 nm each), this provides a proper hole filling and planarization. The second lithography step and following development defines ridge waveguides. After this, SiO_2 cladding is wet etched in BHF, which does not attack SU-8. When etch is completed, specific drying condition is needed to prevent from waveguide collapsing due to capillary forces.
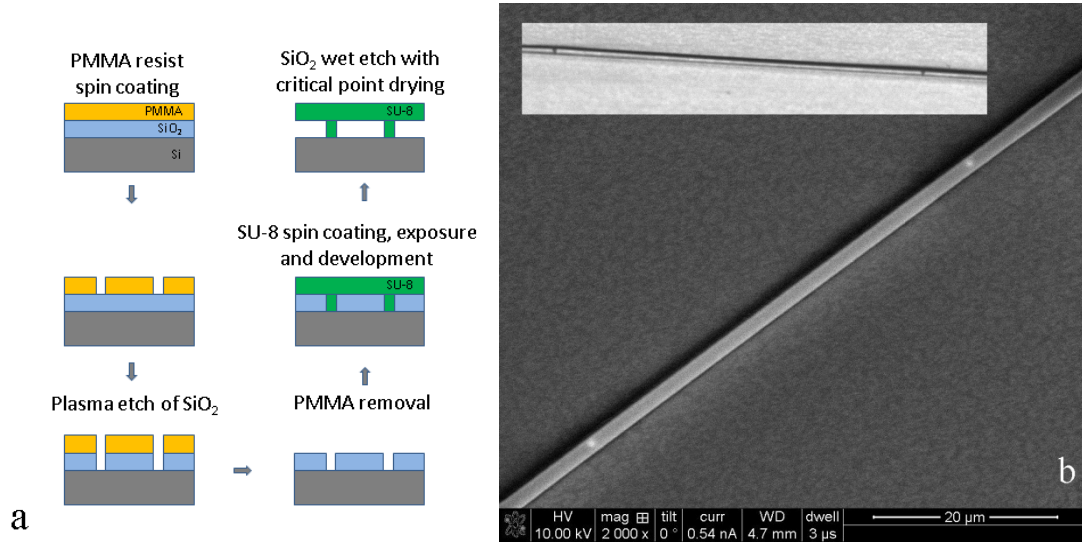
Figure 4.2 Suspended waveguide fabrication route (a) and its top view SEM image (b). Inset shows bridge-like side view of a waveguide.

To avoid this, the sample is immersed in isopropanol and sent to a critical point drying machine, where isopropanol is substituted with liquid CO_2. Under specific temperature and pressure conditions, liquid CO_2 undergoes a critical state where capillary forces are negligible and waveguide release is safe. Figure 4.2b represents a SEM image of a fabricated waveguide. After cleaving with precision diamond scriber samples were sent to a photonic probe station for characterization.

Straight waveguide characterization. Straight waveguides of different lengths (1, 3, 5 mm) were prepared to measure propagation losses and PDL with a cut-back method. Obtained results were compared with analogous measurements of non-suspended waveguides. TE and TM polarized 1550 nm light from a fiber-coupled diode laser was launched into devices and collected with a butt-coupling approach. Collected signal was sent to OSA. PDL were calculated by taking the difference between TE and TM mode propagation losses. Table 4.1 summarizes measurement results.

Table 4.1 Propagation losses and PDL at 1550 nm

	TE, dB/cm	TM, dB/cm	PDL |TE-TM|, dB/cm
Suspended waveguides	2.21±0.15	2.74±0.16	0.53
Non-suspended waveguides	6.52±0.14	11.41±0.15	4.89

As estimated from simulations, dramatic loss decrease is observed for suspended waveguides, especially for TM mode. Polarization sensitivity is decreased from 4.89 dB/cm to 0.53 dB/cm; this value could be further improved by fabricating waveguides with square core profile. Supporting nanopillars are also expected to generate some amount of scattering losses. However, obtained minimal propagation losses of 2.21 dB/cm are still far from applications. But there is a space for improvement up to 0.1 –

0.5 dB/cm loss range typical for rib and channel waveguides while maintaining high integration density of strip waveguides. Possible ways to reach lower propagation losses are to use polymers with less absorption at communication wavelengths and better mechanical properties for a smaller amount of supporting nanopillars; to reduce imperfection concentration by using better fabrication conditions.

Waveguide bending characterization. Waveguides with 90° bending radii ranging from 3 to 20 µm were fabricated and evaluated. As with straight waveguides, non-suspended analogs were also characterized for comparison. Waveguides were designed to have a fixed length. Bending losses were obtained by extracting coupling and propagation losses from total measured loss. Figure 4.3 demonstrates measured and simulated radii dependent bending losses.
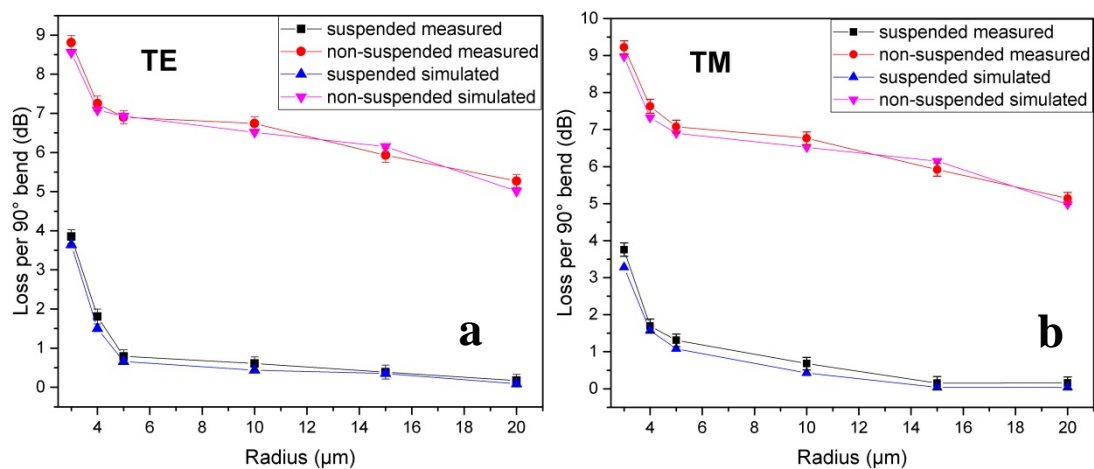

Figure 4.3 Bending losses for TE mode (a) and TM mode (b).

At 15 µm radius bending losses are around 0.15 dB per bend for suspended waveguides, while non-suspended bending with the same radius shows ~6.2 dB which is too lossy for efficient operation. Thus, removal of SiO_2 clad notably decreased low-loss bending radii from more than 100 µm to only 15 µm. Further loss decrease could be achieved by an introduction of an offset between straight waveguide and its curved part to minimize mode transition loss [76]. Together with this, similar range of bending radii as in Si platform is achievable. We also propose more reliable and less expensive approach based on SiO_2 removal under bending region only (Figure 4.4).
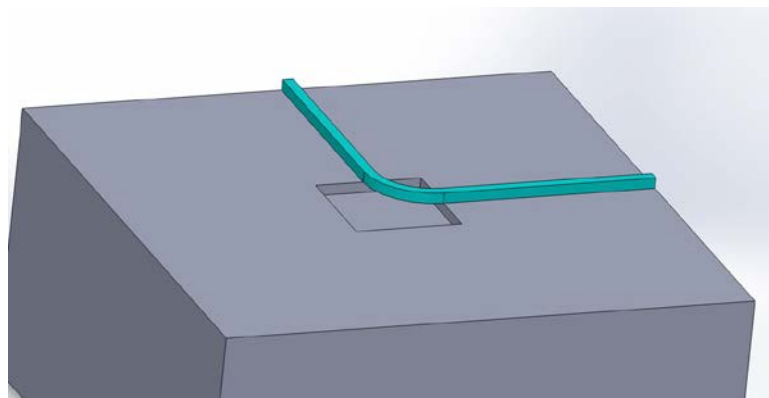

Figure 4.4 Schematic image of a waveguide with bending region being suspended.

4.2 Cylindrical polymer waveguide devices

In comparison with cross-linked SU-8, optical polymers like PMMA exhibit relatively low glass transition temperatures. This feature allows engineering surfaces of microphotonic devices patterned in PMMA. Heating a sample slightly above core polymer T_g changes its viscosity and, consequently, surface roughness and microcracks are reflown due to surface energy change [77]. This is essential for PICs as lower roughness means lower propagation losses. By adjusting thermal treatment conditions, it is also possible to change geometry of fabricated devices. This part demonstrates enhanced optical properties of thermally treated PMMA waveguides and microring resonators.

4.2.1 Reflown waveguides

Similar to previous section, this work aimed to develop polymer optical waveguides with high index contrast, low PDL and propagation losses. In previous work, researchers reported higher effective refractive index in single mode pedestal-standing polystyrene waveguides [78]. In our work, formation of rectangular core profile pedestal-standing PMMA waveguides combined with excessive thermal treatment resulted in circular core waveguides with enhanced light confinement, minimized scattering losses and nearly negligible polarization sensitivity. Similar approach was demonstrated with silica waveguides, however, fabrication is complicated due to high melting point of silica [79]

Numerical 2D simulations of circular core profile waveguide were performed prior to fabrication to study electric field confinement and to ensure single mode light propagation (Figure 4.5a).
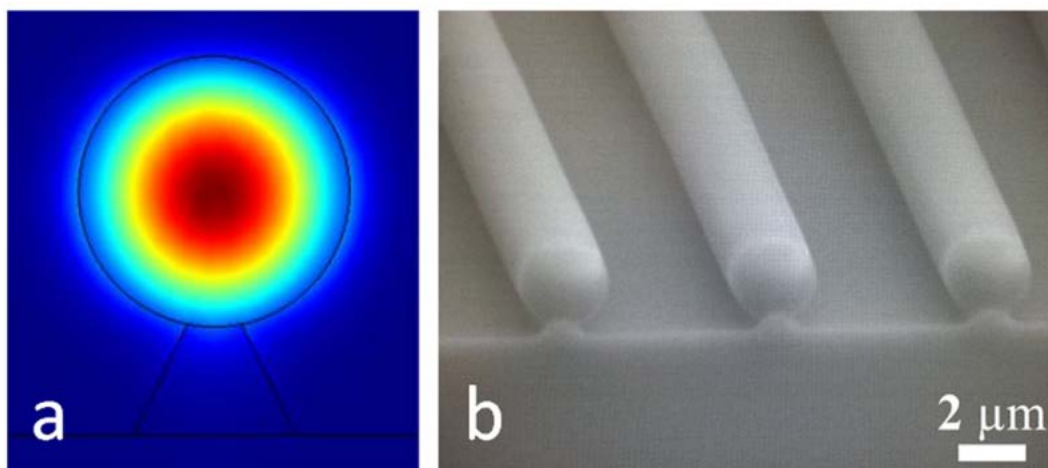

Figure 4.5 FEM mode analysis simulation (a) and SEM image of fabricated cylindrical waveguides (b).

Waveguide diameter of 2.5 μm has shown to be a good compromise between single mode propagation and a tight light confinement. Simulated mode distribution is very similar to one in a single mode optical fiber, so polarization sensitivity of proposed waveguides is expected to be close to zero. Fabricated cylindrical waveguides have nearly perfect circular core profile (Figure 4.5b), so their performance is estimated to be close to simulation results.
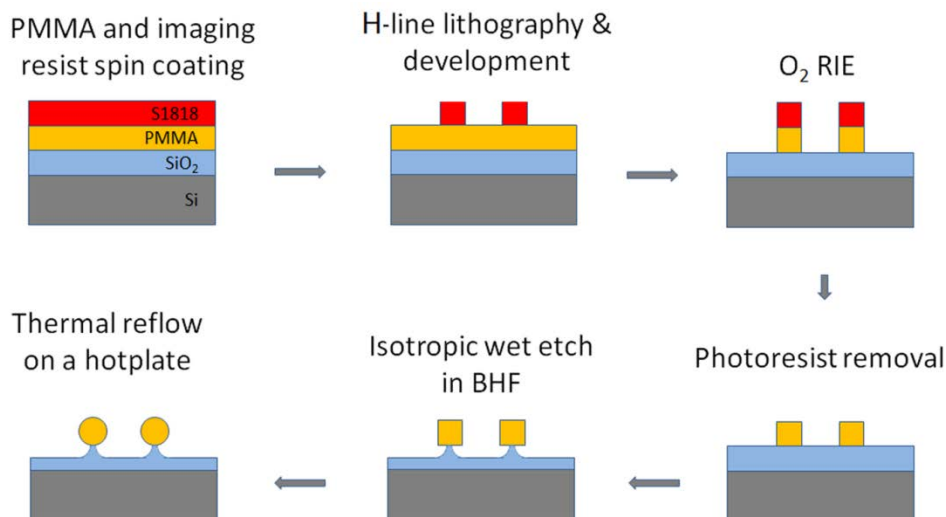

Figure 4.6 Cylindrical waveguide fabrication steps.

Fabrication involved 1 photolithography step, 1 plasma etch, 1 wet etch and a thermal treatment (Figure 4.6). First, PMMA core polymer is spin coated and baked, resulting in 2.5 μm thick film on oxidized Si substrate. SiO_2 cladding thickness is 10 μm. As soon as PMMA is not sensitive to 405 nm light from mercury lamp, 1.8 μm imaging photoresist S1818 (Microposit Corp.) layer is spin coated on top. After 100 mJ/cm^2 exposure in mask aligner and development a sample was sent to O_2 plasma etcher to transfer pattern to PMMA layer. After etch with ~200 nm/min rate is completed, imaging photoresist remains are flood exposed and wet etched away. Then resulting PMMA ridge waveguides are under etched in BHF to form pedestals with ~300 nm width in the upper part. This minimizes waveguide contact area with SiO_2 cladding. Finally, the sample is heated on a hotplate. Careful adjustment of thermal treatment conditions results in a core profile change from rectangular to almost perfectly circular with minimal possible surface roughness.

Characterization of prepared straight cylindrical waveguides included standard propagation loss measurements with cut-back method and PDL measurements [27]. Also, 10 cm long spiral shape waveguide was fabricated and tested as a part of high speed transmission link. For cut-back measurements and PDL 3, 7 and 10 mm waveguides were used. C-band light from a tunable diode laser source was butt-coupled and collected with lensed optical fibers; OSA was used for signal detection. Results from cylindrical waveguides were compared to ones from rectangular waveguides to reveal thermal reflow influence on optical properties. Table 4.2 shows measurement results for 1550 nm.

Table 4.2 Propagation losses and PDL.

	TE, dB/cm	TM, dB/cm	PDL |TE-TM|, dB/cm
Cylindrical waveguides	1.32±0.21	1.40±0.20	~0.08
Rectangular waveguides	1.95±0.21	1.66±0.19	~0.29

From 1535 nm to 1575 nm propagation losses and PDL exhibited negligible variation showing flat broadband operation. As it is seen from Table 4.2, thermal reflow dramatically decreases propagation losses and PDL. Surface roughness induced scattering losses are nearly excluded leaving mostly PMMA intrinsic absorption losses. PDL decreased down to 0.08 dB/cm make reflown waveguides close to polarization insensitive operation which is highly desirable for waveguide-based PIC building blocks like microring resonators, directional couplers, Mach-Zehnder interferometers, etc. However, PMMA exhibits notable absorption at C-band, so we propose demonstrated waveguide treatment method for advanced fluorinated polymers to achieve <0.1 dB/cm propagation losses.

To analyze proposed waveguide performance as a high speed optical interconnect, a 28 Gbaud 64-QAM format modulated optical signal was transmitted through 10 cm long spiral-shape cylindrical waveguide (Figure 4.7a). In this experiment, a transmitter part consists of an external cavity laser and an optical in-phase quadrature (IQ) modulator biased by two synchronized 50 GSa/s arbitrary waveform generators (AWG). An erbium doped fiber amplifier (EDFA) is connected to the output of IQ modulator to amplify 28 Gbaud 64-QAM signal which is then fed to the cylindrical waveguide with a lensed fiber (Figure 4.7b). At the output end of the waveguide the signal is collected with another lensed fiber and sent to an optical signal-to-noise ratio (OSNR) adjusting module. This module consists of a variable optical attenuator and an automatic gain control EDFA; the module is used to sweep different OSNR levels for further OSNR-dependent bit error rate (BER) estimation. After OSNR adjusting module, the signal is sent to a pre-amplifier, band-pass filter and finally to a coherent receiver with narrow linewidth local oscillator laser and a digital storage oscilloscope (DSO, 80 GSa/s, 33 GHz). DSO converts the signal to a digital domain for offline demodulation. Figure 4.6c demonstrates measured BER as a function of OSNR for the tested waveguide and a reference back to back (B2B) transmission. For B2B reference we replaced the polymer waveguide with equivalent insertion loss optical attenuator. In both cases the 28 Gbaud 64-QAM signals achieve BER performance below the 20% overhead soft decision-forward error correction (20% OH SD-FEC) threshold of 2×10^{-2}, yielding error-free post-FEC net bit rate of 140 Gbit/s at single wavelength and polarization (Figure 4.7c-e). With this performance, discussed waveguides can potentially be used in optical signal processing circuits for coherent optical communications. We also propose high performance in direct detection optical links.
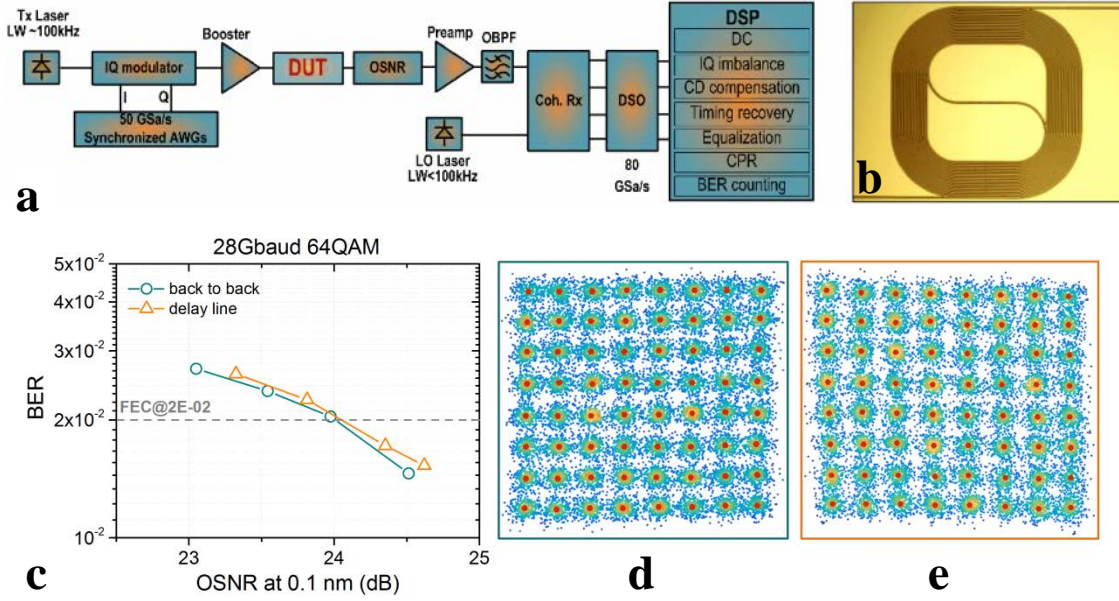
Figure 4.7 High speed transmission experiment link scheme (a) and an optical microscopy image of the tested spiral-shape waveguide (b); BER vs OSNR (c) for 28 Gbaud 64-QAM signal for B2B (d) and the polymer waveguide (e).

4.2.2 Microring resonators

Microring resonators were fabricated and evaluated as an example of devices based on novel cylindrical polymer waveguides. Microring resonators are crucial PIC components used as add-drop filters, delay lines, modulators, etc [58]. Decreased propagation losses and PDL achieved with straight waveguides are promising prerequisites for efficient resonator filtering performance. Microrings and bus waveguides were fabricated with the procedure mentioned before (Figure 4.5c). Among many approaches utilizing e-beam lithography, DUV lithography and nanoimprint lithography (NIL), mercury lamp contact lithography is the most cost-effective solution. However, its resolution limit of ~1 μm is a challenge if submicron control of a coupling gap between microring and bus waveguide is needed. This work demonstrates a change of feature size when thermal reflow reshapes a waveguide profile from rectangular to circular. Considering waveguide cross-section area is constant:

$$hw = \pi\left(\frac{d}{2}\right)^2 \ (4.1)$$

where h and w are rectangular core height and width, respectively, and d is a circular core diameter (Figure 4.8a). Particular initial dimensions lead to waveguide width expansion when reflown. In this case, rectangular waveguide with dimensions $w = 2$ μm and $h = 2.5$ μm turned to circular waveguide with diameter $d \sim 2.53$ μm. So, before reflow a distance between waveguides was 900 nm, but after reflow it narrowed to ~370 nm due to waveguide width expansion (Figure 4.8b). Higher aspect ratio rectangular waveguides would result in even wider lateral expansion.
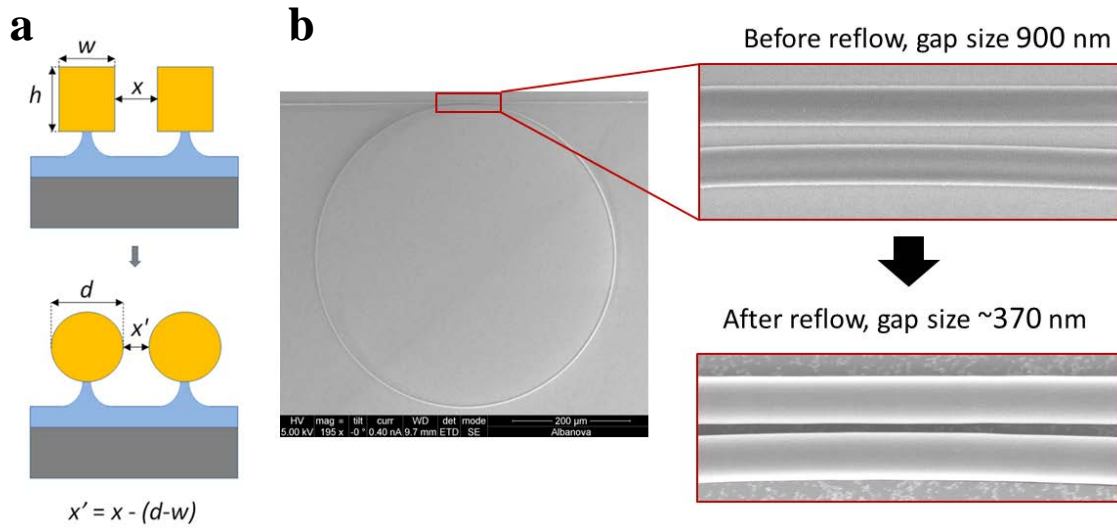
Figure 4.8 Reflow-induced gap narrowing scheme (a) and SEM image of 250 μm radius microring resonator with coupling region magnified (b).

Polymer waveguide treatment method described here allows using inexpensive conventional g-, h-, i-line contact lithography to fabricate sub 400 nm features like a coupling gap of microring resonators or directional couplers.

Cylindrical waveguide and rectangular waveguide resonators were fabricated and characterized in a photonic probe station across C-band to analyze a thermal treatment effect. Figure 4.9a demonstrates transmission spectra of 250 μm radius microring resonator before and after reflow. Two major changes were observed: resonance depth increased from ~ -5 dB to ~ -14 dB indicating increased coupling efficiency as a consequence of coupling gap narrowing. The second change is a quality factor enhancement from 6.41×10^3 to 1.55×10^4 calculated from resonance peak full width at half maximum (FWHM); this is correlated with propagation loss decrease after surface roughness reflow. Polarization-dependent spectra of cylindrical waveguides were obtained by launching TE and TM modes (Figure 4.9b). Despite straight waveguides have shown nearly negligible PDL, there is a resonance peak shift between TE and TM spectra. The shift is approximately 10% from free spectral range (FSR) which is 1.2 nm for 500 μm diameter microring. Such polarization dependency could be crucial for some applications; we propose thermal tuning with a microheater as a possible way to compensate observed peak shift and notch depth.

To summarize, proposed here post-processing thermal treatment notably enhances waveguide performance. Higher refractive index contrast and propagation loss decrease accompanied by nearly negligible PDL are highly desirable for efficient performance as a part of PICs.
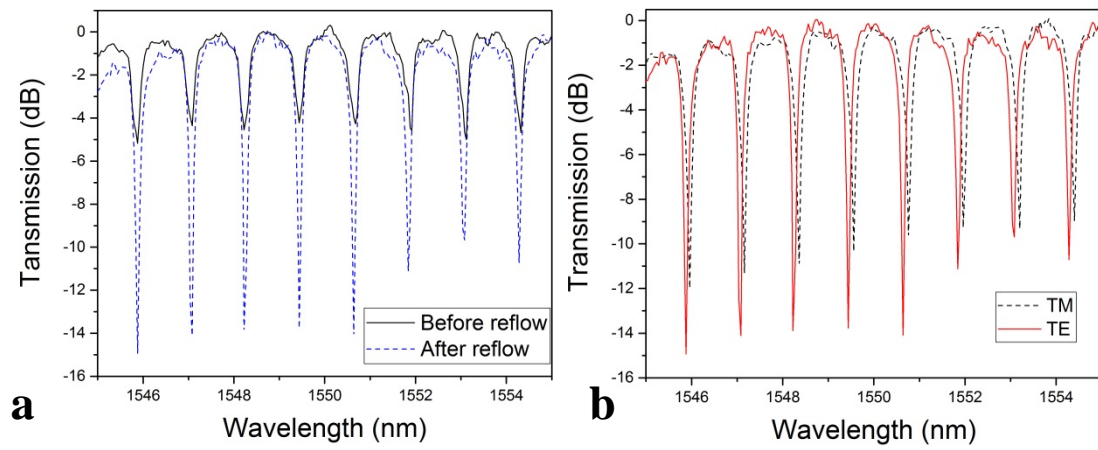
Figure 4.9 Normalized TE mode transmission of a microring before and after reflow (a), TE and TM mode transmission of reflown resonator (b).

Chapter 5

5 Active hybrid polymer/Si nanocrystal devices and materials

This chapter presents active polymer waveguide devices and materials. Active properties are introduced by doping polymers with Si nanocrystals which exhibit a wide range of interesting optical properties thanks to quantum confinement effect in 0D materials. Potentially, Si NC dopings provide light emission, light amplification, sensitization of rare earth ions, light modulation, etc. Section 5.1 focuses on all-optical modulation induced by free carrier absorption (FCA) in PMMA waveguides doped with Si NCs **(Paper C).** Sections 5.2 and 5.3 reveal detailed analysis of Si NC optical properties in different polymer matrices **(Papers D and E).** The research of hybrid polymer/Si NC nanocomposites brings novel materials with advanced functionality to the field of integrated photonics.

5.1 Si NC doped PMMA strip waveguides

Si NCs are getting more and more attention as an active material for integrated photonics. Numerous applications employing Si NCs on-chip were demonstrated: all-optical FCA modulation in microring resonators [80], light emission from whispering gallery mode (WGM) cavities [81], four wave mixing (FWM) in Si NC doped waveguides [82], etc. Si NCs demonstrate χ^3 nonlinearity order of magnitude higher than one of a bulk Si [52, 83]. However, reported devices are based on SiO_x, Si_3N_4 platforms employing complex plasma deposition equipment. To decrease fabrication costs, inexpensive Si NC chemical synthesis and easy-processable optical polymer platform is preferable. Potentially, polymer platform offers higher nonlinear performance as a cumulative effect of Si NCs and nonlinear polymer matrix. Optical polymers with nonlinear properties several orders of magnitude higher than ones of SiO_2, Si_3N_4 and Si are commercially available [84].

In this work, all-optical FCA modulation in PMMA waveguides doped with Si NCs is investigated. Previous work shows notable signal quenching by free carriers in Si NCs generated by optical excitation [85]. FCA loss coefficient can be theoretically obtained from the following equation:

$$\alpha_{FCA} = \sigma_{FCA} \times N_{exc} = -\frac{1}{\Gamma L}\left(\frac{P_{probe\,with\,pump}}{P_{probe\,w/o\,pump}}\right) \quad (5.1)$$

where σ_{FCA} is a FCA cross-section, N_{exc} is an excited free carrier concentration, Γ is

an optical confinement factor, L is a waveguide length, $P_{\text{probe with pump}}$ and $P_{\text{probe w/o pump}}$ are output powers with and without pump laser excitation, respectively.

To prepare active waveguide material, PMMA powder with a molecular weight of 950k was dissolved in toluene. Then, ~5 nm size dodecene-passivated Si NC toluene colloid was added and properly mixed. Resulting Si NC concentration is ~0.1% by mass of solid PMMA. To fabricate active waveguides, prepared Si NC/PMMA toluene solution was spin-coated on Si substrate with 10 μm thermally grown oxide, which serves as a cladding. After 140° C 2 min soft-bake on a hotplate the active polymer film with 2.5 μm thickness is ready. Next, waveguide pattern is defined with e-beam lithography at a dose of 210 μC/cm^2. Based on numerical simulations, waveguide dimensions were chosen to be 3 μm in width and 2.5 μm high. FEM mode analysis ensures a single mode propagation of a probe signal and demonstrates a good light confinement (~90% of total power). This provides a proper interaction of optical mode and Si NCs. After development and chip cleavage waveguides are ready for characterization. Figure 5.1 shows some parameters of prepared waveguides.
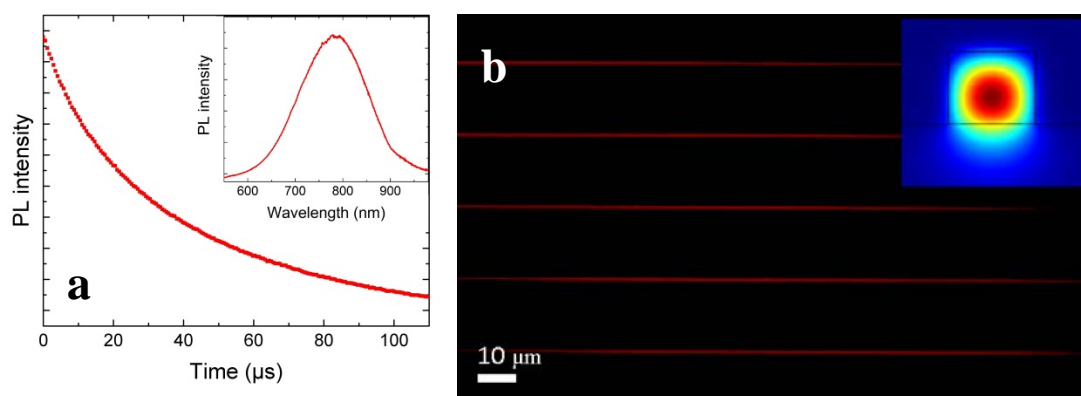

Figure 5.1 Si NC/PMMA waveguide PL decay curve, inset shows PL spectrum (a); optical microscopy image of fabricated waveguides under UV light excitation, inset shows FEM simulation of probe signal mode distribution (b).

Both PL spectrum and lifetime did not change significantly after transition from colloid to solid PMMA matrix, indicating that encapsulation process did not affect optical stability of Si NCs. Pump and probe setup for time-resolved FCA modulation in integrated waveguides was developed (Figure 5.2). 1550 nm probe signal from fiber-coupled diode laser was launched into waveguides and collected with lensed fibers; active waveguides were vertically pumped from a free-space with 405 nm CW laser diode at different power levels, a pump intensity was modulated with a mechanical chopper. A focused pump spot was shaped into ~100 μm wide 5 mm long stripe. The output probe signal was sent to a fiber-coupled InGaAs photodetector and further analyzed in electrical domain using an oscilloscope. Cut-back measurements without pumping demonstrated passive propagation loss of ~1.8±0.2 dB/cm for TE mode. For FCA induced loss measurements 5 mm long waveguides were excited at 405 nm with powers ranging from 10 mW/cm^2 to 100 mW/cm^2. As expected, probe signal is quenched when Si NCs are excited. Generated electron-hole pairs absorb probe photons to push electrons to higher energy level in Si NC conduction band.
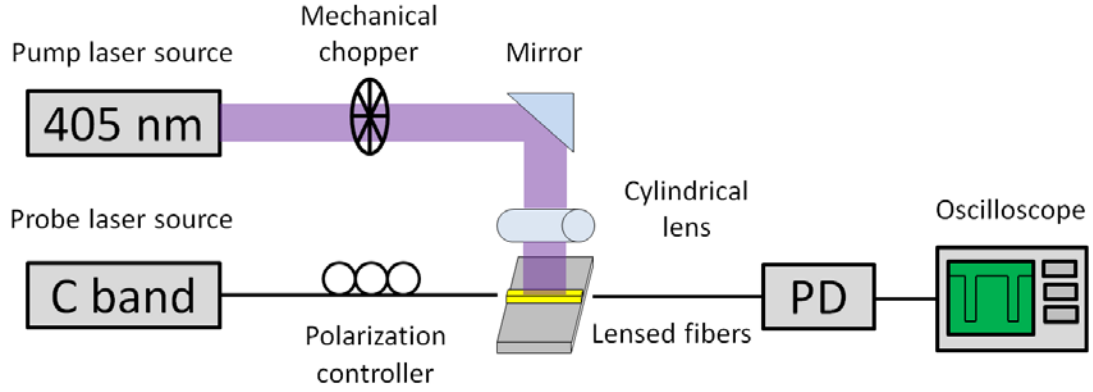
40

Figure 5.2 All-optical modulation experimental setup.

As seen from Figure 5.3a, a modulation depth of 1.55 dB is achieved at maximum pumping power. Probe signal drop and recovery dynamics after excitation pulse are in a good agreement with previously done carrier lifetime measurements, indicating tens of µs relaxation times (Figure 5.3b). Signal drop takes ~75 µs and recovery is ~125 µs, yielding few kHz modulation speed. This is the main bandwidth limitation in such devices, carriers cannot be extracted from a waveguide due to matrix dielectric behavior. One could try conductive waveguide matrices. Using experimentally obtained data, calculated α_{FCA} is 1.6 cm^{-1} which is a promising result since only 0.1% by mass Si NC concentration was studied here. To compare, related works with Si NCs in inorganic matrices utilize 6-27% Si concentration [85, 86].

Demonstrated active waveguides are potential candidates for low-cost all-optical switching components where few kHz switching frequency is needed.
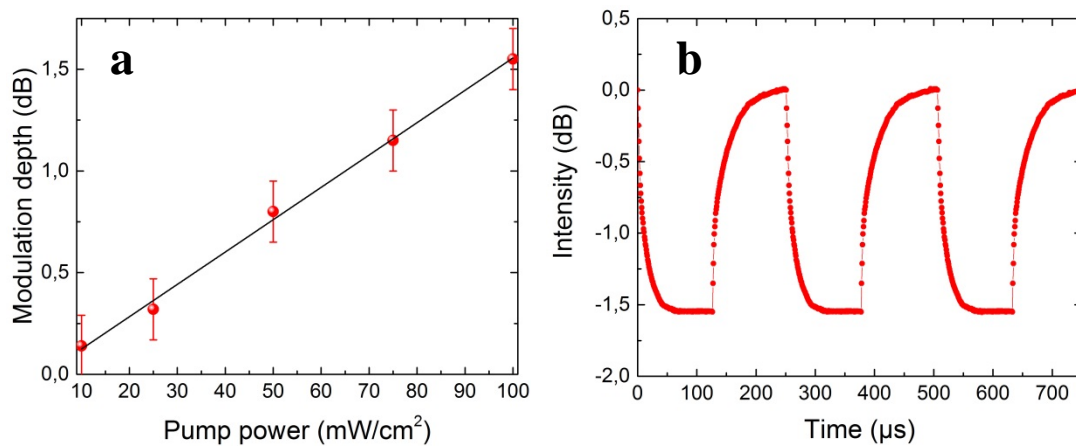

Figure 5.3 Modulation depth as a function of pump power with a linear fit (a) and 4 kHz intensity modulation at 100 mW/cm^2 power (b).

5.2 Si NCs in PMMA

As soon as integrated polymer optical devices doped with Si NCs are promising candidates for a variety of applications, a proper analysis of hybrid polymer/Si NC materials is needed. Unlike Si NCs in SiO_2 thin films, prepared by clearly physical methods, Si NCs processed by chemical methods allow inexpensive large quantity synthesis and widely tunable properties [87]. A key parameter that determines a performance of active semiconductor device is a quantum yield. In ideal device, all electron-hole pairs emit photons when recombine. Si NCs in SiO_2 rarely exceed 20% QY, i.e. only 1 out of 5 excitons produce a photon [88]. Non-radiative recombinations occur due to defects in oxide which serve as electron traps [89]. Chemical synthesis methods provide organically-capped Si NC colloids with more efficient surface passivation. QYs of such ensembles are approaching 60% [90]. Clearly, it is favorable to transfer Si NCs with so attractive optical properties into solid transparent matrix. Optical polymers seem to be perfect candidates for such hybrid system thanks to low cost and well-studied synthesis routines. In this work, we encapsulated free-standing Si NCs prepared by chemical route into PMMA bulk matrix and evaluated optical properties of fabricated PMMA/Si NC hybrid materials.

We fabricated bulk quantities of hybrid materials to repetitively study QY in integrating sphere and to prove a concept of suitability for mass fabrication. Integrating sphere method is hardly applicable to thin films due to small NC quantities. Also, we studied carrier lifetime dynamics. We evaluated optical stability of prepared hybrids by repeating measurements in predetermined time intervals and monitoring optical performance changes.

In our research we used Si NCs prepared through thermal anneal of hydrogen silsesquioxane (HSQ) resulting in Si NCs in SiO_2 matrix. Next, obtained brownish powder was etched in HF to release H-terminated Si NCs with hydrophobic properties. After etching was finished, hydrophobic NCs were extracted with toluene. Resulting Si NC/toluene colloid is ready for use. However, hydride passivation obtained from HF etch has poor stability and is prone to oxidation and Si-H bond scission. As a result, optical properties degrade in several days. Another surface passivation is needed to stabilize optical properties; functionalization with alkenes is an effective approach. Si NCs were functionalized with alkenes by radical driven reaction called hydrosilylation, photostability over years is confirmed [91]. We investigated encapsulation of both hydride- and alkene-passivated nanoparticles in a PMMA matrix. We started with dodecene-terminated Si NCs, see Figure 5.4.
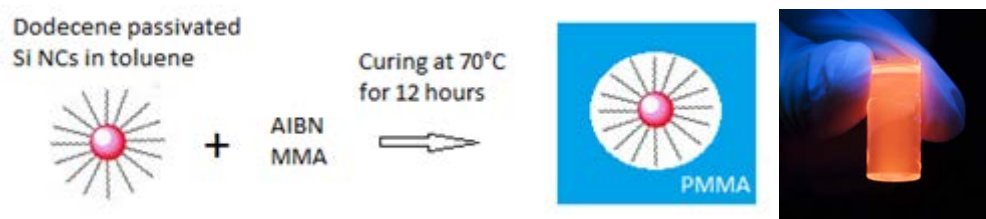

Figure 5.4 PMMA/Si NC nanocomposite synthesis from dodecene-functionalized NCs (a) and a photograph of resulting sample under UV light (b).

To synthesize discussed hybrids, dodecene-passivated Si NC/toluene colloid was added to liquid monomer (monomethyl acrylate, MMA) together with polymerization reaction initiator (azobisisobutyronitrile, AIBN) and reaction vial was kept at 70° C for 12 hours. After release from a glass vial, ~ 4 ml volume sample is ready for characterization. We used two batches of different size Si NCs with different photoluminescence spectra peaks and called them "red" and "orange" according to their color under UV light illumination. In both samples Si NC concentration is roughly $10^{14\text{-}15}$ particles per cm^3. We measured PL spectra, absolute QY and carrier lifetimes before and after encapsulation and repeated measurements over time to investigate a photostability of prepared hybrids (Figure 5.5).
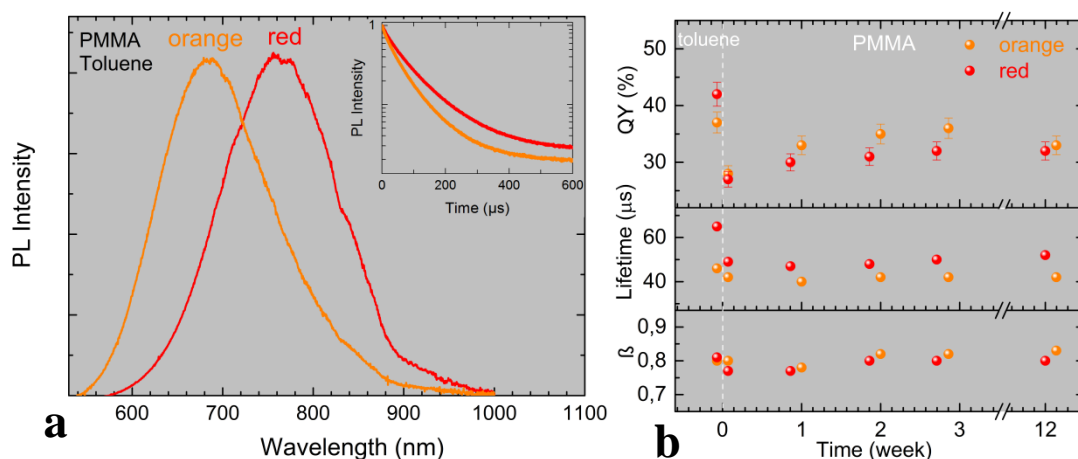

Figure 5.5 PL spectra of two dodecene-passivated samples with different PL peaks; inset shows their decay curves (a). Progress of absolute QY, carrier lifetime and decay dispersion factor β upon encapsulation in PMMA (b).

PL spectra of both samples did not change after encapsulation in PMMA (Figure 5.5a). Broad spectra indicate Si NC size distribution in ensemble. To analize PL decay, a stretched exponential function was used :

$$I = I_0 \exp(-(\frac{t}{\tau})^\beta \quad (3.1)$$

where τ is a lifetime and β is a dispersion factor that represents a variation of individual lifetimes due to size distribution of NCs. A decrease of τ and β indicates introduction of new non-radiative processes that lower internal quantum efficiency. So, absolute QY, τ and β monitoring can reveal photostability of samples. Immediately after encapsulation both samples show parameter drop, however, partial recovery over time is observed. After few months hybrids stabilize at 30-40% QY without any change in PL spectra.

Alkene passivation provides good optical stability, but certain PL tunability limitation takes place due to oxygen diffusion and Si NC surface oxidation at functionalization stage. Oxygen-related surface traps limit PL to red-NIR region while hydride-terminated Si NCs show size-dependent PL spectrum tunability across the whole visible range without a presence of oxygen.
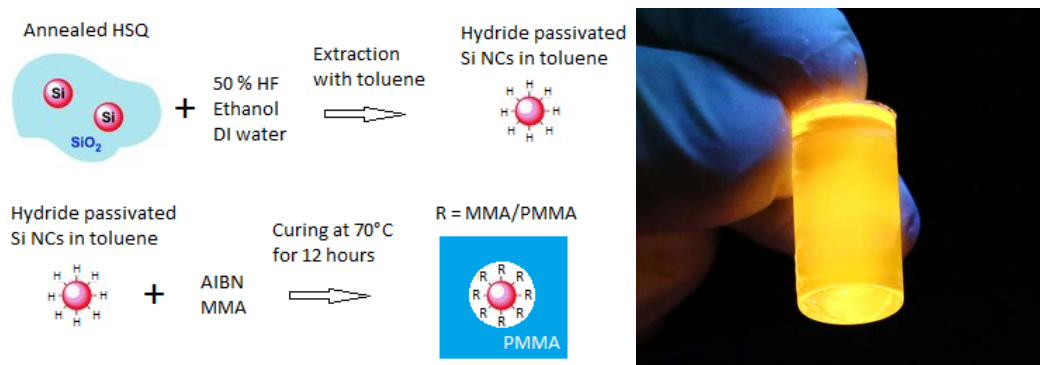
Figure 5.6 PMMA/Si NC nanocomposite synthesis from hydride-functionalized NCs (a) and a photograph of resulting sample under UV light (b).

So, after successful encapsulation of dodecene-passivated NCs, we decided to encapsulate as-prepared hydride-terminated NCs (Figure 5.6). As soon as MMA polymerization utilizes same radical chemistry as Si NC hydrosilylation process, encapsulation of H-terminated NCs involves two parallel reactions: MMA polymerization into PMMA and Si NC surface functionalization with MMA/PMMA molecules. In this way, separate passivation step is avoided. Together with PL tunability via particle size, this is a promising approach for relatively easy bulk quantity fabrication of hybrid material with tunable optical properties.
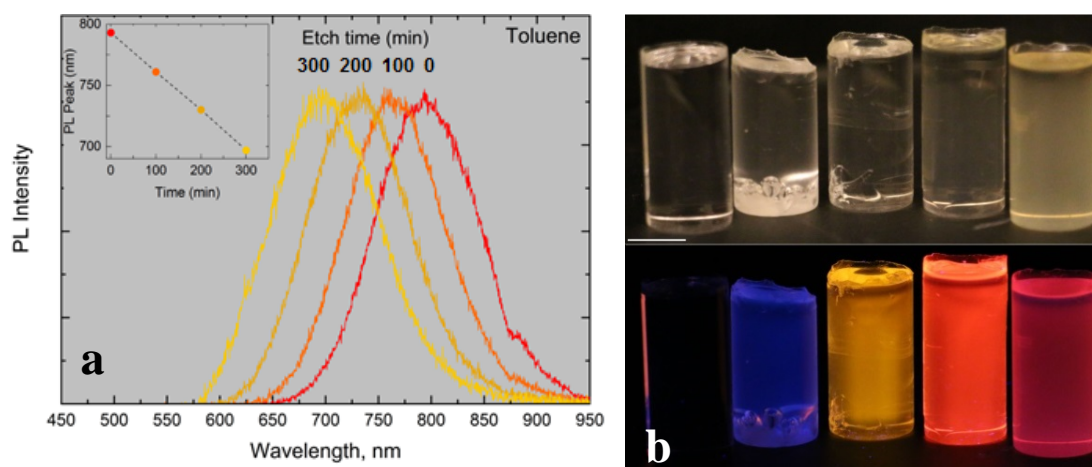
Figure 5.7 Etch time dependent PL spectra (a); prepared samples under ambient light (b, top) and UV light (b, bottom). Scale bar length is 1 cm.

A size tuning was performed through photo-assisted etch in HF. After H-terminated NCs are released from SiO_2 and extracted with toluene, there are still some traces of HF remaining. We illuminated such Si NC/toluene colloid with 3W 575 nm LED and measured PL spectra with time intervals (Figure 5.7a). After PL peak tuning NCs were cleaned in fresh toluene, precipitated and encapsulated into PMMA (Figure 5.7b). Prepared nanocomposites were optically characterized with the same methods as samples derived from dodecene-passivated Si NCs (Figure 5.8).

Figure 5.8 PL spectra of H-terminated Si NCs before and after encapsulation in PMMA, inset shows a SEM image of a cleaved sample surface (a). Evolution of hybrid optical properties over time (b).

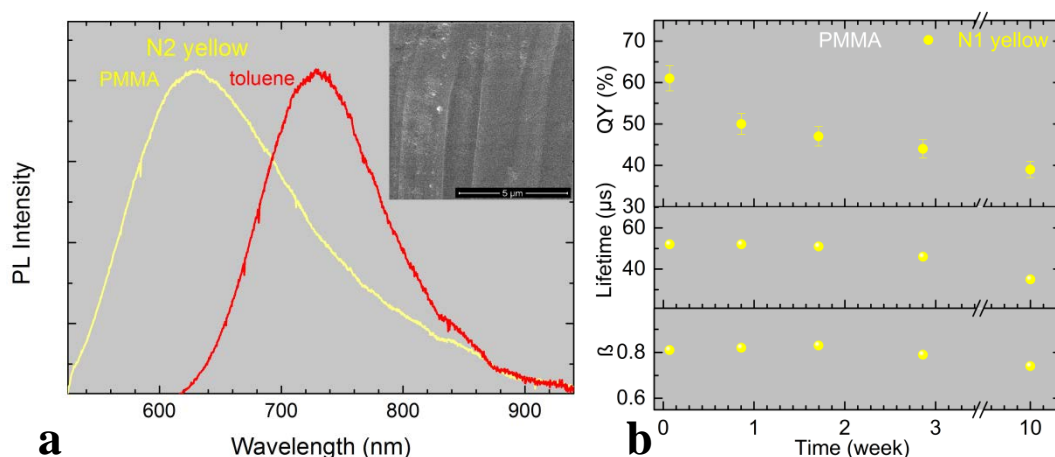In contrast to hybrids from dodecene-functionalized Si NCs, PL spectra of hybrids derived from H-NCs markedly blue-shifted after polymerization. One of the possible reasons is etching with residual HF during polymerization process. However, spectra show stability over months since polymerization reaction finishes. This supports a hypothesis that hydride termination was exchanged to MMA/PMMA ligands similarly to passivation with dodecene molecules, since both polymerization and Si NC functionalization reactions are driven by free radicals from AIBN [92]. A QY decreased from ~60% to ~45% after first 3 weeks, this can be attributed to a cleavage of H-Si bonds that were not exchanged with MMA/PMMA during encapsulation. Si NCs with such dangling bonds turn "dark" and contribute to non-radiative recombinations, decreasing an absolute QY. Lifetime and β experienced slight decrease indicating new possible non-radiative recombination channels, probably due to diffusion of oxygen and subsequent NC surface oxidation. Thus, nevertheless some initial degradation takes place, stable 30-40% QY hybrids with yellow-orange PL are obtained. Inset in Figure 5.8a demonstrates a SEM image of a cleaved sample surface showing no porosity at imaging resolution. Vertical grooves originate from internal stresses induced by polymerization and released during cleavage indicate that prepared material behaves like a monolithic solid, not like porous structure. So, at least to some extent Si NCs are protected from interactions with environment.

We also investigated a possibility to obtain blue-green emitting hybrids by encapsulating H-Si NCs photo-etched for longer times. Fabricated samples show substantially different optical properties than hybrids described in previous section. Poor 7% QY measured directly after encapsulation dropped to ~1% after few days, decay rate is in the range of nanoseconds (~10^4 times faster than yellow-red hybrids, Figure 5.9). Judging from these dramatically different properties, we assume there are another recombination mechanisms rather than one from quantum confinement effect in Si. Similar PL was observed in porous Si and SiO_2 defects [93, 94]. Taking into account synthesis was conducted under unprotected atmosphere, we attribute such behavior to oxide defect PL from partially and fully oxidized Si NCs.
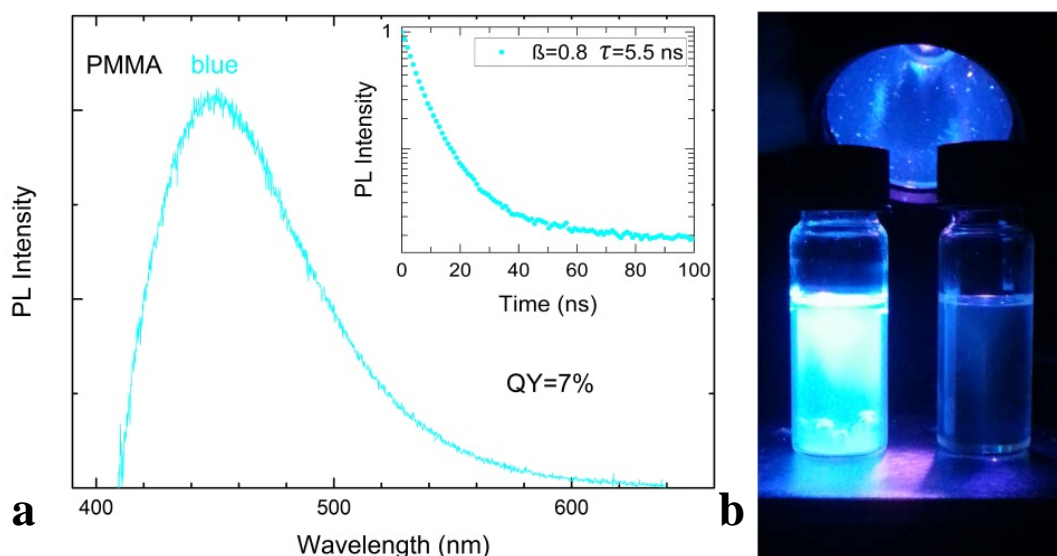
Figure 5.9 PL spectra of blue-emitting sample, inset shows its decay rate (a) and a photograph together with a reference sample (b).

Finally, we demonstrated a low complexity fabrication of hybrid active material with stable (30-40% QY) tunable PL in yellow-NIR spectrum part. Another notable property of prepared hybrids is a large Stokes shift of Si NCs originating from indirect bandgap of bulk Si. Together with low absorption in PMMA, this results in fair transparency at optical communication wavelengths.

5.3 Si NCs in thiol-ene polymer

Encouraged by results obtained with Si NC/PMMA materials, we explored encapsulation of Si NCs into other polymer matrices. We aimed for more reactive chemistry to effectively co-passivate dodecene-terminated NCs and for more convenient polymerization process. Off-stoichiometry thiol-ene (OSTE) polymers were a matrix of choice thanks to their extremely fast UV-induced polymerization rates, low shrinkage, tunable mechanical and chemical properties, and highly mobile reactive radicals capable of Si NC dangling bond passivation. With moderate power UV light source, it takes only tens of seconds to polymerize few cm^3 volume of OSTE [45]. To compare, it took ~12 hours to produce PMMA of the same volume. This is crucial as soon as industry requires fast large quantity fabrication of bulk materials.

Thiol-based ligands were extensively used for direct bandgap quantum dots, however, did not bring sufficiently good results with Si NCs [95]. Thiol-ene polymerization reaction is driven by highly mobile UV-activated thiyl radicals, which in turn can produce carbon-centered radicals from allyls. Both are theoretically capable of Si NC non-radiative center passivation making NC optically active and leading to increased ensemble QY.

Scheme 5.1. UV curing of OSTE polymer together with Si NC co-passivation process.
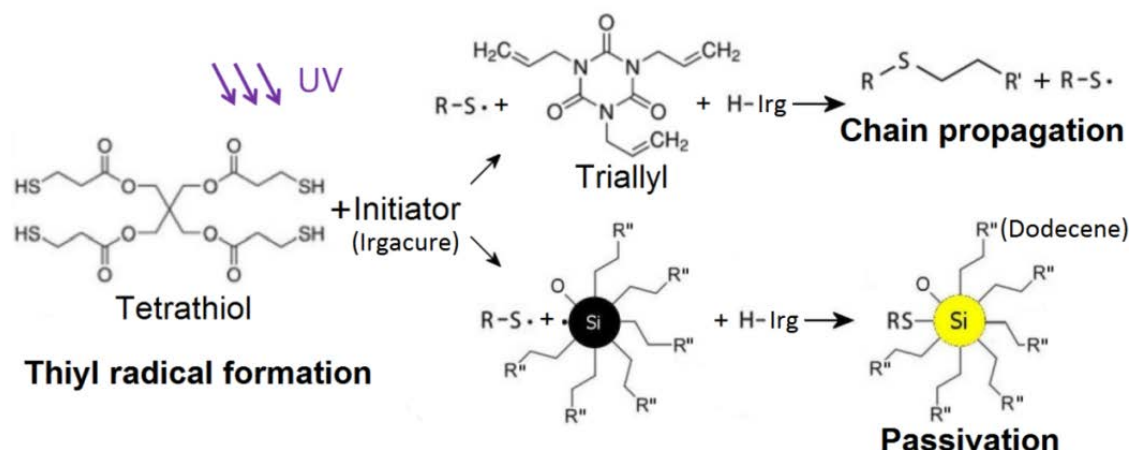
We hypothesize that OSTE radicals contribute to both polymerization and dangling bond passivation, so these 2 processes run in parallel. Scheme 5.1 demonstrates polymerization reaction together with one of the possible Si NC dangling bond co-passivation mechanisms. The polymerization step-growth reaction is based on addition of a thiol group (-SH) to an ene group (C=C). OSTE radical concentrations can be indirectly alternated by changing initial thiol and ene (allyl) monomer ratio [96]. This approach was originally used to tune chemical and mechanical properties of OSTE polymers.

In our experiments, we fabricated Si NC/OSTE hybrid materials by adding ~5 nm size dodecene-capped Si NCs toluene colloid to thiol/allyl monomer blend with a photoinitiator (Irgacure 184). We kept Si NC concentration at 0.01% by mass for all samples. It normally took 20s to fully cure ~3 ml samples under 12 mW/cm^2 collimated Hg lamp light (~ 350-450 nm). When Si NCs were encapsulated into formulations with excess thiols, notable QY increase was observed: for example, from 20-30% as a colloid to 40-50% as a polymer/Si NC hybrid (Figure 5.10a). We attribute obtained QY enhancement to effective co-passivation of dangling bonds by thiyl and carbon radicals in OSTE. Indeed, Si NC passivation with thiol ligands was already reported, but exhibited low QYs and poor stability. In our case, fabricated samples demonstrate QY stability over several months. After encapsulation, PL spectra remain mostly unchanged except for appearance of fine features caused by PL reabsorption in matrix (Figure 5.10b). A dip at ~1.42 eV (~875 nm) on Si NC in toluene spectrum corresponds to a specific toluene absorption band (overtone of a C-H stretching mode in toluene molecule) [97]. It is clearly seen that this dip disappears after encapsulation into OSTE, however, another feature appears at ~1.37 eV (~905 nm, slight slope change of red curve in Figure 5.10b). It represents a specific OSTE molecule overtone absorption band. Reabsorbed PL was estimated to be less than 1% of total emission, so this phenomenon does not affect QY calculation significantly. Finally, by analyzing such fine features of spectra in NIR region it is possible to reveal a sample composition to some extent.
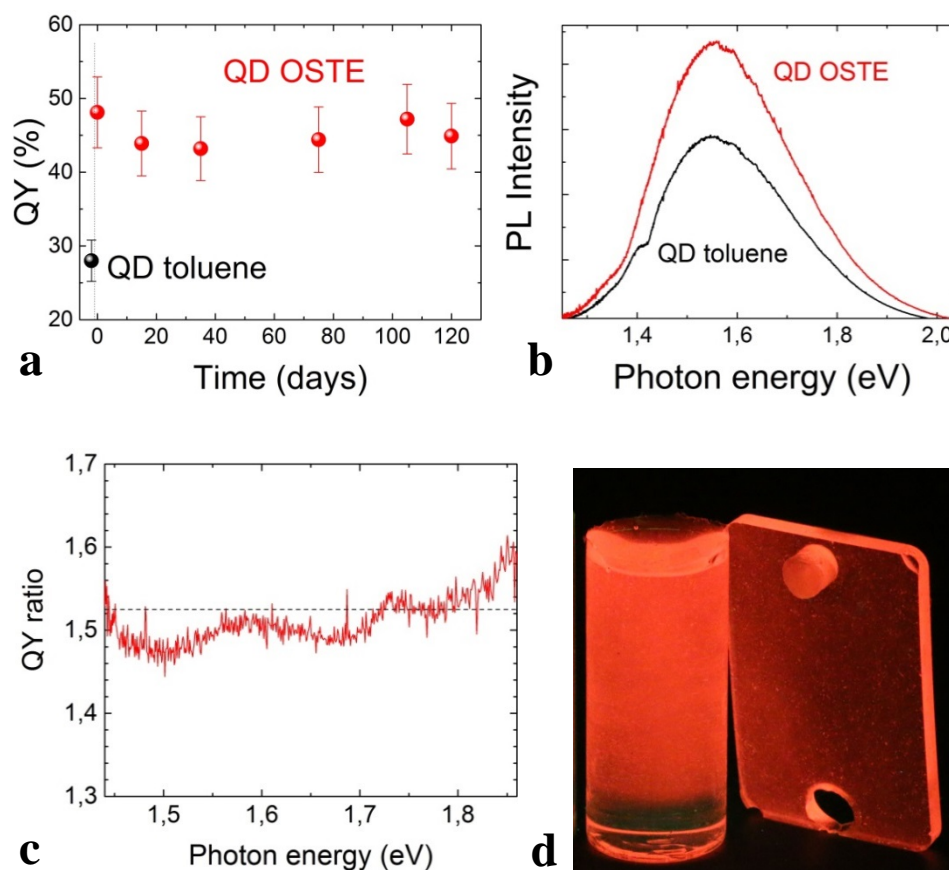
Figure 5.10 QY increase after transfer from toluene (black dot) to OSTE (40% thiol excess, red dots) as a function of shelf life time (a). PL spectra of Si NC colloid (black curve) and Si NC/OSTE hybrid (red curve) under equal excitation conditions (b). The proportion between spectra in (b) showing uniform QY enhancement (c). A photograph of prepared hybrid samples under UV light (d).

To verify our hypothesis based on co-passivation with highly mobile OSTE radicals, we prepared a set of test samples with varying thiol/allyl off-stoichiometry (0% to 100% thiol excess, which is 2:1 thiol/allyl group ratio; and the same for allyl excess). According to reported theoretical investigation, higher excess of thiols results in higher concentrations of both thiyl radicals and carbon-centered radicals. Figure 5.11a shows that increasing thiol excess results in higher QY values, in line with our theory proposing that higher active radical concentrations provide more complete co-passivation of non-radiative centers. Allyl excess experiments demonstrate a slight drop of QY with increasing allyl fraction, indicating that less active radicals were available for co-passivation (Figure 5.11b). Unfortunately, direct detection of new bonds on Si NC surfaces is a non-trivial task due to extremely low amount of co-passivated Si vacancies. It could be a single reacted bond per thousands of atoms on Si NC surface that makes a NC optically active. Therefore, FTIR and X-ray photoelectron spectroscopy (XPS) cannot provide any reliable information here.
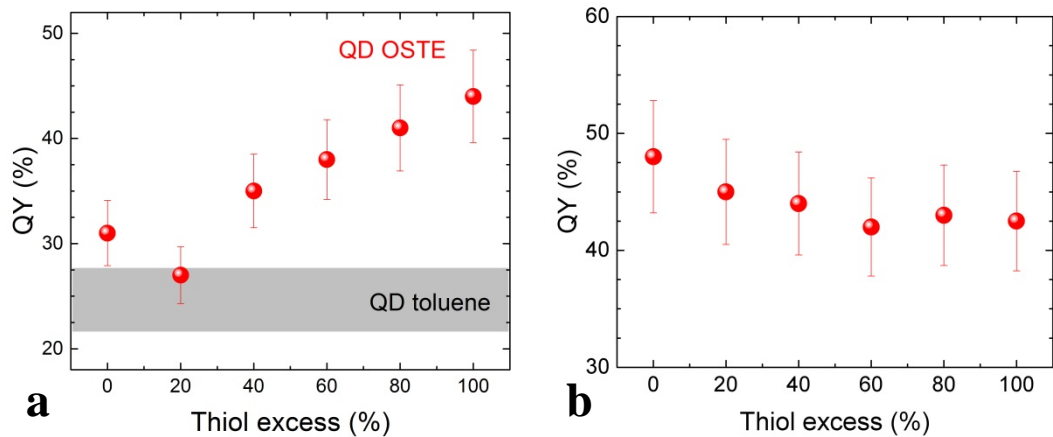
Figure 5.11 QY dependent on thiol (a) and allyl (b) excess; note that Si NCs colloids with different initial QY were used: 20-30% for thiol excess and 40-50% for allyl excess.

To verify optical stability, additional spectrally resolved measurements of decay rates ($1/\tau$) and β were performed (Figure 5.12). These parameters remain largely unchanged after encapsulation into OSTE. High β values indicate an absence of new non-radiative channels introduced by polymerization, therefore, NCs in a hybrid are either bright or dark. This is consistent with a hypothesis stating that QY increase is attributed to an increase of bright particle fraction.
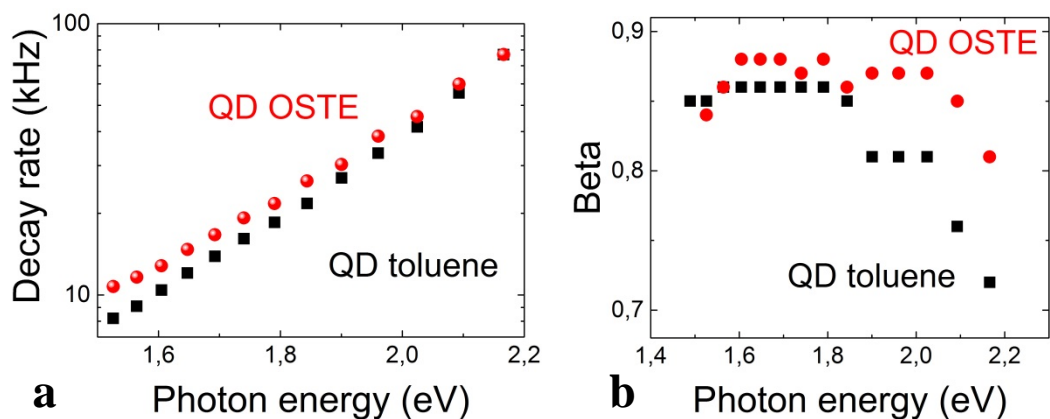
Figure 5.12 Decay rate (a) and β (b) of a sample with 40% thiol excess (Figure 5.10) in comparison to Si NC colloid.

There are two major ways to introduce free radicals to start polymerization and hydrosilylation reactions: with a photoinitiator and with an ionizing irradiation. A photoinitiator used in this work (Irgacure 184) has a strong absorption in UV and partially blue spectral region, overlapping with Si NC absorption (Figure 5.13a). The photoinitiator remaining after polymerization can decrease optical pump efficiency, so initiator-free samples were also prepared to achieve higher matrix transparency in UV-blue spectrum part (Figure 5.13b). Such samples were prepared by sandwiching monomer blend with Si NCs between two 4 inch fused silica wafers and exposing to deep UV light (180 mJ/cm^2 of UVC light). Silica wafers were pre-treated with SH-functionalized sylane to ensure a good adhesion with OSTE. High transparency, rapid

polymerization and low shrinkage make OSTE outperform PMMA traditionally used as a matrix for quantum dots. Stable 60-70% QY of Si NCs encapsulated in OSTE matrix allows implementing developed hybrid material not only as active material for integrated photonics, but also as glass laminates for sun energy harvesting devices like luminescent solar concentrators [98].

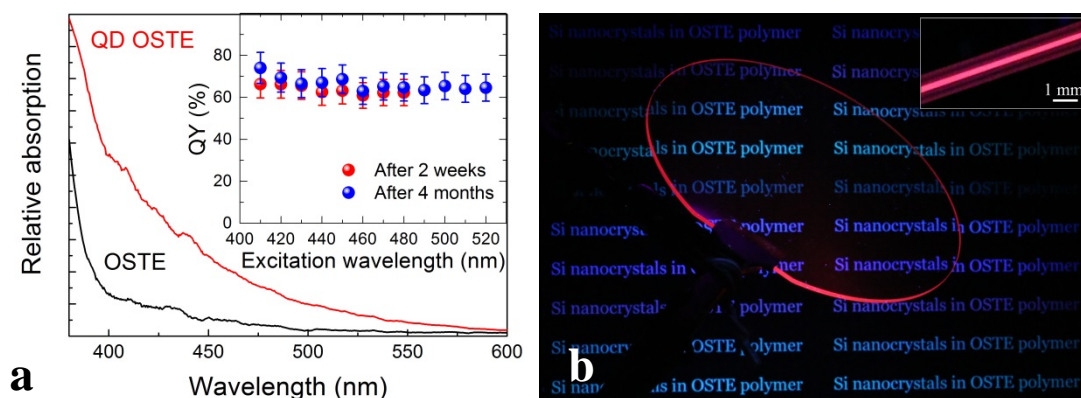Figure 5.13 Wavelength dependent absorption of OSTE polymer and Si NC/OSTE hybrid, both prepared with a photoinitiator. Inset shows pump wavelength independent ~65% QY sample stable over 4 months (a). A photograph of initiator-free highly transparent Si NC/OSTE glass laminate, it is seen that optical spectrum transmission through such laminate is not affected. Inset shows a magnified laminate side view (b).

Chapter 6

6 Conclusions and future work

6.1 Conclusions

In summary, in this thesis we propose and develop passive and active integrated polymer waveguides for PICs; we report novel optical materials based on Si QDs embedded in polymers as well.

Polymer photonics platform was introduced and compared with other PIC material systems. After discussion of advantages of optical polymers, problems are noted and routes to their reduction are proposed. Novel Si QD doped polymers with broad functionality are discussed.

A theoretical background on light propagation in polymer PICs and semiconductor physics of quasi-direct bandgap Si NCs is briefly presented. A working principle of integrated component simulation tools such as FEM and FDTD is described with examples given.

A fabrication of polymer PICs in clean room environment is presented with a description of standard tools used in semiconductor industry: lithography, plasma etching, polymer thin film preparation, etc. Characterization procedures for polymer chips are explained, from optical inspection with a microscope to transmission experiments on a photonic probe station, where a signal from single-mode optical fiber is butt-coupled to integrated waveguides. Chemical synthesis routes of different Si NC/polymer nanocomposites are presented, a quantum yield and free carrier lifetime analysis principles are explained and measurement setup schemes provided.

Novel approaches to enhance polymer waveguide performance are presented. We show a study on 1550 nm light propagation in air-suspended SU-8 waveguides. A removal of SiO_2 cladding underneath waveguides provides better light confinement (uniform refractive index contrast of ~57.5%) and smaller sensitivity to light polarization. Both simulation results and experimental evaluation show a decrease of low-loss 90° bending radius from >100 μm to ~15 μm, which greatly reduces PIC footprint and gives more freedom in PIC design.

We investigated an influence of thermal treatment on PMMA waveguides and microring resonators. By heating close to a glass transition temperature, a surface of PMMA waveguides standing on thin SiO_2 pedestals is reflown and scattering losses are reduced from ~2 dB/cm to ~1.3 dB/cm. Heating-induced polymer viscosity change provides a waveguide profile change from rectangular to a circular; this greatly improves waveguide insensitivity to light polarization (PDL decreased from ~0.3 dB/cm to less than 0.1 dB/cm). Consequently, thermal reflow enhances a Q-factor of microring resonators up to ~2 times. Also, reflow-induced <400 nm coupling gap between microring and bus waveguide is demonstrated with inexpensive contact lithography tool, avoiding use of sophisticated techniques like e-beam lithography.

Active polymer waveguides for all-optical intensity modulation are developed. Addition of Si NCs into PMMA waveguides allows active functions like signal intensity modulation based on free carrier absorption effect. The concentration of free carriers in Si NCs is altered by pumping with UV light pulses from a free space. Intensity modulation down to -1.55 dB was experimentally shown for 5 mm long devices. Free carrier relaxation time is determined to be a major modulation bandwidth limiting factor.

Hybrid Si NC/polymer materials for active applications are synthesized and characterized.

Si NCs were embedded into PMMA by thermal polymerization of MMA - Si NC colloid. NCs of different sizes were used to produce nanocomposites with different PL peaks. Stable over several months 30-40% QY and free carrier lifetimes for hybrids with PL in yellow-NIR range reported. Another type of developed nanocomposites is fabricated by encapsulating Si NCs into OSTE polymer. Reactivity of OSTE monomers allows rapid polymerization (10-20 s for ~3 cm^3 volume) and Si NC surface reactions that increase a QY and photostability. Record high ~65% QY among any reported to date solid state Si NC composites is reported.

6.2 Future work

We propose the following future work in the field of integrated polymer photonics:
- Development of higher refractive index polymers with high transparency in optical communication windows. An achievement of Si_3N_4 refractive index level would greatly decrease polymer device footprint while keeping low fabrication complexity and chip costs. At the same time, polymers with very low refractive index are also desirable as a cladding material to achieve a high index contrast.
- Experimental demonstration of stable organic chromophore self-alignment in polymers. Considering electric field poling is a non-trivial procedure with limited efficiency, self-assembled hybrids would be extremely beneficial as materials with high 2nd order non-linearity. This would push a development of electro-optical modulators based on Pockels effect.
- Research on Si NC and other QD encapsulation in polymers. Surface chemistry here defines optical properties and overall dopant efficiency. This is crucial to implement on-chip polymer amplifiers.
- Investigations on conductive polymers to implement light sources and photodetectors on a polymer chip.

Summary of Appended Papers

A. **Aleksandrs Marinins,** Nicolas Knudde and Sergei Popov, "Air-suspended SU-8 strip waveguides with high refractive index contrast", IEEE Photonics Technology Letters, v. 34 (17), pp. 1862-1865, 2016.
   Contribution: design, fabrication and characterization; part of simulation; greater part of manuscript writing.

B. **Aleksandrs Marinins,** Oskars Ozolins, Xiaodan Pang, Aleksejs Udalcovs, Jaime Rodrigo Navarro, Aditya Kakkar, Richard Schatz, Gunnar Jacobsen and Sergei Popov, "Thermal reflow engineered cylindrical polymer waveguides for optical interconnects", submitted to IEEE Photonics Technology Letters, 2017.
   Contribution: design, simulation and fabrication; part of characterization; greater part of manuscript writing.

C. **Aleksandrs Marinins,** Oskars Ozolins, Xiaodan Pang, Aleksejs Udalcovs, Gunnar Jacobsen, Ilya Sychugov, Jan Linrros and Sergei Popov, "Free carrier absorption modulation in polymer waveguides doped with Si nanocrystals", manuscript prepared, 2017.
   Contribution: design, simulation, fabrication and characterization; greater part of manuscript writing.

D. **Aleksandrs Marinins,** Zhenyu Yang, Hongzheng Chen, Jan Linnros, Jonathan G.C. Veinot, Sergei Popov and Ilya Sychugov, "Photostable Polymer/Si Nanocrystal Bulk Hybrids with Tunable Photoluminescence", ACS Photonics, v. 3 (9), pp. 1575-1580, 2016.
   Contribution: fabrication; part of concept, characterization and manuscript writing.

E. **Aleksandrs Marinins,** Reza Zandi Shafagh, Wouter van der Wijngaart, Tommy Haraldsson, Jan Linnros, Jonathan G. C. Veinot, Sergei Popov and Ilya Sychugov, "Light Converting Polymer/Si Nanocrystal Composites with Stable 60-70% Quantum Efficiency and Their Glass Laminates", DOI: 10.1021/acsami.7b09265.
   Contribution: fabrication; part of concept, characterization and manuscript writing.

References

[1]   E. Fortunato, P. Barquinha, and R. Martins, "Oxide semiconductor thin-film transistors: A review of recent advances," *Adv. Mater.,* vol. 24, no. 22, pp. 2945-2986, 2012.

[2]   T. Li, "Optical Fiber Communication—The State of the Art," *IEEE Transactions on Communications,* vol. 26, no. 7, pp. 946-955, 1978.

[3]   W. B. Bielawski, "LOW-LOSS OPTICAL WAVEGUIDES: CURRENT STATUS," *Electro-Opt Syst Des,* vol. 5, no. 4, pp. 22-28, 1973.

[4]   R. J. Mears, L. Reekie, I. M. Jauncey, D. N. Payne, and R. J. Mears, "Low-noise erbium-doped fibre amplifier operating at 1.54μm," *Electron. Lett.,* vol. 23, no. 19, pp. 1026-1028, 1987.

[5]   D. Kalish and L. G. Cohen, "SINGLE-MODE FIBER: FROM RESEARCH AND DEVELOPMENT TO MANUFACTURING," *AT&T Technical Journal,* vol. 66, no. 1, pp. 19-32, 1987.

[6]   M. Glick, "The role of integrated photonics in datacenter networks," in *Proceedings of SPIE - The International Society for Optical Engineering*, 2017, vol. 10131.

[7]   K. Yamada *et al.*, "High-performance silicon photonics technology for telecommunications applications," *Science and Technology of Advanced Materials,* vol. 15, no. 2, 2014.

[8]   K. Williams, "InP Integrated photonics: State of the art and future directions," in *2017 Optical Fiber Communications Conference and Exhibition, OFC 2017 - Proceedings*, 2017.

[9]   S. Hurtt *et al.*, "The first commercial large-scale InP photonic integrated circuits: Current status and performance," in *65th DRC Device Research Conference*, 2007, p. 183.

[10]   H. Kataria, W. T. Metaferia, C. Junesand, C. Zhang, J. E. Bowers, and S. Lourdudoss, "High quality large area ELOG InP on silicon for photonic integration using conventional optical lithography," in *Proceedings of SPIE - The International Society for Optical Engineering*, 2014, vol. 8989.

[11]   X. Wang and R. T. Chen, "Recent progress on polymer photonics and optical interconnects," in *2008 Asia Optical Fiber Communication and Optoelectronic Exposition and Conference, AOE 2008*, 2008.

[12]   D. A. P. Bulla, B. V. Borges, M. A. Romero, N. I. Morimoto, L. G. Neto, and A. L. Cortes, "Design and fabrication of SiO2/Si3N4 CVD optical waveguides," in *SBMO/IEEE MTT-S International Microwave and Optoelectronics Conference Proceedings*, 1999, vol. 2, pp. 454-457.

[13]   A. Yeniay, R. Gao, K. Takayama, R. Gao, and A. F. Garito, "Ultra Low Loss Polymer Waveguides," in *Conference on Optical Fiber Communication, Technical Digest Series*, 2003, vol. 86, pp. 902-904.

[14]   S. Takenobu and Y. Morizawa, "Long spiral optical waveguides using ultra low loss perfluorinated polymer for optical interconnect," in *Conference on Optical Fiber Communication, Technical Digest Series*, 2009.

[15]   M. Kleinert *et al.*, "Photonic integrated devices and functions on hybrid polymer platform," in *Proceedings of SPIE - The International Society for Optical Engineering*,

2017, vol. 10098.

[16]   N. Keil *et al.*, "Ultra low-loss 1×2 multiplexer using thin-film filters on polymer integration platform," *Electron. Lett.,* vol. 45, no. 23, pp. 1167-1168, 2009.

[17]   M. Happach *et al.*, "Temperature-Tolerant Wavelength-Setting and-Stabilization in a Polymer-Based Tunable DBR Laser," *J. Lightwave Technol.,* vol. 35, no. 10, pp. 1797-1802, 2017.

[18]   D. De Felipe *et al.*, "Recent Developments in Polymer-Based Photonic Components for Disruptive Capacity Upgrade in Data Centers," *J. Lightwave Technol.,* vol. 35, no. 4, pp. 683-689, 2017.

[19]   J. Gosciniak, D. T. H. Tan, and B. Corbett, "Enhanced performance of graphene-based electro-absorption waveguide modulators by engineered optical modes," *J. Phys. D: Appl. Phys.,* vol. 48, no. 23, 2015.

[20]   H. Gordillo, I. Suarez, R. Abargues, P. Rodriguez-Canto, G. Almuneau, and J. P. Martinez-Pastor, "Quantum-dot double layer polymer waveguides by evanescent light coupling," *J. Lightwave Technol.,* vol. 31, no. 15, pp. 2515-2525, 2013.

[21]   M. Lee *et al.*, "Broadband modulation of light by using an electro-optic polymer," *Science,* vol. 298, no. 5597, pp. 1401-1403, 2002.

[22]   L. T. Canham, "Silicon quantum wire array fabrication by electrochemical and chemical dissolution of wafers," (in English), *Appl. Phys. Lett.,* vol. 57, no. 10, pp. 1046-1048, Sep 1990.

[23]   B. Delley and E. F. Steigmeier, "Quantum confinement in Si nanocrystals," *Physical Review B,* vol. 47, no. 3, pp. 1397-1400, 1993.

[24]   M. Dasog, J. Kehrle, B. Rieger, and J. G. C. Veinot, "Silicon nanocrystals and silicon-polymer hybrids: Synthesis, surface engineering, and applications," *Angewandte Chemie - International Edition,* vol. 55, no. 7, pp. 2322-2339, 2016.

[25]   E. A. J. Marcatili, "Dielectric Rectangular Waveguide and Directional Coupler for Integrated Optics," *Bcl] Syst. Tech. J.,* vol. 48, no. 7, pp. 2071-2102, 1969.

[26]   E. A. J. Marcatili, "What kind of optical fiber for long-distance transmission?," *Proceedings of SPIE - The International Society for Optical Engineering,* vol. 21, pp. 7-21, 1970.

[27]   J. L. Jackel and J. J. Veselka, "Measuring losses in optical waveguides: A new method," *Appl. Opt.,* vol. 23, no. 2, pp. 197-199, 1984.

[28]   F. P. Payne and J. P. R. Lacey, "A theoretical analysis of scattering loss from planar optical waveguides," *Optical and Quantum Electronics,* vol. 26, no. 10, pp. 977-986, 1994.

[29]   X. Sun *et al.*, "Optimized inductively coupled plasma etching for poly(methyl-methacrylate- glycidly-methacrylate) optical waveguide," *Thin Solid Films,* vol. 520, no. 18, pp. 5946-5951, 2012.

[30]   L. A. Coldren, S. W. Corzine, and M. L. Masanovic, "Diode lasers and photonic integrated circuits," *John Wiley Sons, Inc., Hoboken, New Jersey,* 2012.

[31]   H. Ma, A. K. Y. Jen, and L. R. Dalton, "Polymer-based optical waveguides: Materials, processing, and devices," *Adv. Mater.,* vol. 14, no. 19, pp. 1339-1365, 2002.

[32]   B. R. Bennett, R. A. Soref, and J. A. Del Alamo, "Carrier-Induced Change in Refractive Index of InP, GaAs, and InGaAsP," *IEEE J. Quantum Electron.,* vol. 26, no. 1, pp. 113-122, 1990.

[33]   D. Dai, L. Liu, S. Gao, D. X. Xu, and S. He, "Polarization management for silicon photonic integrated circuits," *Laser and Photonics Reviews,* vol. 7, no. 3, pp. 303-328, 2013.

[34]   F. E. Doany *et al.*, "Terabit/s-class optical PCB links incorporating 360-Gb/s bidirectional 850 nm parallel optical transceivers," *J. Lightwave Technol.,* vol. 30, no.

4, pp. 560-571, 2012.

[35]   J. Hu, L. Li, H. Lin, P. Zhang, W. Zhou, and Z. Ma, "Flexible integrated photonics: Where materials,mechanics and optics meet [Invited]," *Optical Materials Express,* vol. 3, no. 9, pp. 1313-1331, 2013.

[36]   S. Takenobu *et al.*, "A polymer waveguide material optimized for on-board optical links and Si photonic interfaces," in *Optics InfoBase Conference Papers*, 2017, vol. Part F40-OFC 2017.

[37]   M. Kleinert *et al.*, "Recent progress in InP/polymer-based devices for telecom and data center applications," in *Proceedings of SPIE - The International Society for Optical Engineering*, 2015, vol. 9365.

[38]   B. M. A. Rahman, N. Somasiri, and K. T. V. Grattan, "Birefringence compensation of silica waveguides," *IEEE Photonics Technology Letters,* vol. 17, no. 6, pp. 1205-1207, 2005.

[39]   J. Zhou, W. H. Wong, N. Q. Ngo, E. Y. B. Pun, Y. Q. Shen, and Y. X. Zhao, "Polymer-based waveguides with low propagation loss and polarization- dependent loss," *Optics and Laser Technology,* vol. 37, no. 6, pp. 427-431, 2005.

[40]   A. Boersma *et al.*, "Polymer-based optical interconnects using nanoimprint lithography," in *Proceedings of SPIE - The International Society for Optical Engineering*, 2013, vol. 8630.

[41]   J. W. Kang, J. P. Kim, W. Y. Lee, J. S. Kim, J. S. Lee, and J. J. Kim, "Low-loss fluorinated poly(arylene ether sulfide) waveguides with high thermal stability," *J. Lightwave Technol.,* vol. 19, no. 6, pp. 872-875, 2001.

[42]   Y. Zhao *et al.*, "Cross-linkable fluorinated poly(ether ether ketone) polymers for optical waveguide devices," *Mater. Lett.,* vol. 58, no. 19, pp. 2365-2368, 2004.

[43]   M. Hikita, R. Yoshimura, M. Usui, S. Tomaru, and S. Imamura, "Polymeric optical waveguides for optical interconnections," *Thin Solid Films,* vol. 331, no. 1-2, pp. 303-308, 1998.

[44]   M. Nordström, D. A. Zauner, A. Boisen, and J. Hübner, "Monolithic single mode SU-8 waveguides for integrated optics," in *Proceedings of SPIE - The International Society for Optical Engineering*, 2006, vol. 6112.

[45]   C. F. Carlborg, T. Haraldsson, K. Öberg, M. Malkoch, and W. Van Der Wijngaart, "Beyond PDMS: Off-stoichiometry thiol-ene (OSTE) based soft lithography for rapid prototyping of microfluidic devices," *Lab on a Chip,* vol. 11, no. 18, pp. 3136-3147, 2011.

[46]   S. E. Thompson and S. Parthasarathy, "Moore's law: the future of Si microelectronics," *Mater. Today,* vol. 9, no. 6, pp. 20-25, 2006.

[47]   G. Allan and C. Delerue, "Efficient intraband optical transitions in Si nanocrystals," *Phys. Rev. B,* vol. 66, no. 23, Dec 15 2002.

[48]   M. L. Brongersma, P. G. Kik, A. Polman, K. S. Min, and H. A. Atwater, "Size-dependent electron-hole exchange interaction in Si nanocrystals," *Appl. Phys. Lett.,* vol. 76, no. 3, pp. 351-353, Jan 17 2000.

[49]   A. D. Yoffe, "Semiconductor quantum dots and related systems: Electronic, optical, luminescence and related properties of low dimensional systems," *Adv. Phys.,* vol. 50, no. 1, pp. 1-208, 2001.

[50]   J. Heitmann, F. Müller, L. Yi, M. Zacharias, D. Kovalev, and F. Eichhorn, "Excitons in Si nanocrystals: Confinement and migration effects," *Physical Review B - Condensed Matter and Materials Physics,* vol. 69, no. 19, pp. 195309-195301-195309-195307, 2004.

[51]   M. Dasog, G. B. De Los Reyes, L. V. Titova, F. A. Hegmann, and J. G. C. Veinot, "Size vs Surface: Tuning the Photoluminescence of Freestanding Silicon Nanocrystals

Across the Visible Spectrum via Surface Groups," *ACS Nano,* vol. 8, no. 9, pp. 9636-9648, 2014.

[52] H. Yildirim and C. Bulutay, "Enhancement of optical switching parameter and third-order optical nonlinearities in embedded Si nanocrystals: A theoretical assessment," *Opt. Commun.,* vol. 281, no. 15-16, pp. 4118-4120, 2008.

[53] Y. Kanemitsu and S. Okamoto, "Phonon structures and Stokes shift in resonantly excited luminescence of silicon nanocrystals," *Physical Review B - Condensed Matter and Materials Physics,* vol. 58, no. 15, pp. 9652-9655, 1998.

[54] https://optiwave.com/resources/academia/free-fdtd-download/.

[55] https://www.comsol.com/.

[56] K. Chandrashekar and G. V. Attimarad, "Analysis of electromagnetic wave propagation at discontinuities for different dielectric waveguide geometries using two-dimensional FEM," in *International Conference on Trends in Automation, Communication and Computing Technologies, I-TACT 2015*, 2016.

[57] N. Goto and Y. Miyazaki, "Finite-difference time-domain analysis of wavelength-selective characteristics in weighted acoustooptic switches for wavelength-division-multiplexed photonic routing," *Japanese Journal of Applied Physics, Part 1: Regular Papers and Short Notes and Review Papers,* vol. 43, no. 5 B, pp. 2958-2964, 2004.

[58] W. Bogaerts *et al.*, "Silicon microring resonators," *Laser and Photonics Reviews,* vol. 6, no. 1, pp. 47-73, 2012.

[59] http://microchem.com/pdf/PMMA_Data_Sheet.pdf.

[60] T. Okino, Y. Kuba, M. Shibata, and H. Ohyi, "130 kV high-resolution electron beam lithography system for sub-10-nm nanofabrication," *Jpn. J. Appl. Phys.,* vol. 52, no. 6 PART 2, 2013.

[61] H. I. Smith, "A review of submicron lithography," *Superlattices Microstruct.,* vol. 2, no. 2, pp. 129-142, 1986.

[62] E. B. Graper, "Evaporation characteristics of materials from an electron beam gun II," *Journal of Vacuum Science and Technology A: Vacuum, Surfaces and Films,* vol. 5, no. 4, pp. 2718-2723, 1987.

[63] http://www.oxfordplasma.de/systems/100ll.htm.

[64] H. Toyoda, H. Komiya, and H. Itakura, "Etching characteristics of SiO2 in CHF3 gas plasma," *J. Electron. Mater.,* vol. 9, no. 3, pp. 569-584, 1980.

[65] K. R. Williams, K. Gupta, and M. Wasilik, "Etch rates for micromachining processing - Part II," *Journal of Microelectromechanical Systems,* vol. 12, no. 6, pp. 761-778, 2003.

[66] G. L. Weibel and C. K. Ober, "An overview of supercritical CO2 applications in microelectronics processing," *Microelectron. Eng.,* vol. 65, no. 1-2, pp. 145-152, 2002.

[67] R. A. Minns and R. A. Gaudiana, "Design and synthesis of high refractive index polymers. II," *Journal of macromolecular science. Chemistry,* vol. A29, no. 1, pp. 19-30, 1992.

[68] J. C. De Mello, H. F. Wittmann, and R. H. Friend, "An improved experimental determination of external photoluminescence quantum efficiency," *Adv. Mater.,* vol. 9, no. 3, pp. 230-232, 1997.

[69] F. Sangghaleh, B. Bruhn, T. Schmidt, and J. Linnros, "Exciton lifetime measurements on single silicon quantum dots," *Nanotechnology,* vol. 24, no. 22, 2013.

[70] F. Sangghaleh, I. Sychugov, Z. Yang, J. G. C. Veinot, and J. Linnros, "Near-Unity Internal Quantum Efficiency of Luminescent Silicon Nanocrystals with Ligand Passivation," *ACS Nano,* vol. 9, no. 7, pp. 7097-7104, 2015.

[71] http://www.nanonics.co.il/our-products/lens-fiber-probes.

[72] R. Bruck and R. Hainberger, "Efficient small grating couplers for low-index difference

waveguide systems," in *Proceedings of SPIE - The International Society for Optical Engineering*, 2009, vol. 7218.

[73]   L. Eldada, C. Xu, K. M. T. Stengel, L. W. Shacklette, and J. T. Yardley, "Laser-fabricated low-loss single-mode raised-rib waveguiding devices in polymers," *J. Lightwave Technol.,* vol. 14, no. 7, pp. 1704-1712, 1996.

[74]   H. Lorenz, M. Despont, N. Fahrni, N. LaBianca, P. Renaud, and P. Vettiger, "SU-8: A low-cost negative resist for MEMS," *Journal of Micromechanics and Microengineering,* vol. 7, no. 3, pp. 121-124, 1997.

[75]   B. Yang, Z. Sheng, and D. Dai, "Design of suspended SU-8 optical waveguides for ultrasmall bending," in *Proceedings of SPIE - The International Society for Optical Engineering*, 2009, vol. 7630.

[76]   L. D. Hutcheson and J. J. Burke, "Comparison of bending losses in integrated optical circuits," *Optics Letters,* vol. 5, no. 6, pp. 276-278, 1980.

[77]   C. Y. Chao and L. J. Guo, "Reduction of surface scattering loss in polymer microrings using thermal-reflow technique," *IEEE Photon. Technol. Lett.,* vol. 16, no. 6, pp. 1498-1500, 2004.

[78]   C. Y. Chao, W. Fung, and L. J. Guo, "Polymer microring resonators for biochemical sensing applications," *IEEE J. Sel. Top. Quantum Electron.,* vol. 12, no. 1, pp. 134-142, 2006.

[79]   A. J. Maker and A. M. Armani, "Low-loss silica-on-silicon waveguides," *Opt. Lett.,* vol. 36, no. 19, pp. 3729-3731, 2011.

[80]   B. J. Huang *et al.*, "All-optical cross-absorption-modulation based Gb/s switching with silicon quantum dots," *IEEE Journal on Selected Topics in Quantum Electronics,* vol. 22, no. 6, 2016.

[81]   R. D. Kekatpure and M. L. Brongersma, "Fundamental photophysics and optical loss processes in Si-nanocrystal-doped microdisk resonators," *Physical Review A - Atomic, Molecular, and Optical Physics,* vol. 78, no. 2, 2008.

[82]   S. Manna *et al.*, "Stimulated degenerate four-wave mixing in Si nanocrystal waveguides," *Journal of Optics (United Kingdom),* vol. 18, no. 7, 2016.

[83]   C. L. Wu *et al.*, "Enriching Si quantum dots in a Si-rich SiNx matrix for strong χ(3) optical nonlinearity," *Journal of Materials Chemistry C,* vol. 4, no. 7, pp. 1405-1413, 2016.

[84]   http://www.tcichemicals.com/eshop/en/ns/category_index/12986/.

[85]   Y. Lebour, D. Navarro-Urrios, P. Pellegrino, G. Sarrabayrouse, L. Pavesi, and B. Garrido, "Optical amplification studies in Si nanocrystals-based waveguides prepared by ion-beam synthesis," *Physica E: Low-Dimensional Systems and Nanostructures,* vol. 41, no. 6, pp. 1044-1047, 2009.

[86]   R. D. Kekatpure and M. L. Brongersma, "Quantification of free-carrier absorption in silicon nanocrystals with an optical microcavity," *Nano Lett.,* vol. 8, no. 11, pp. 3787-3793, 2008.

[87]   C. M. Hessel, E. J. Henderson, and J. G. C. Veinot, "Hydrogen Silsesquioxane: A Molecular Precursor for Nanocrystalline Si-SiO2 Composites and Freestanding Hydride-surface-terminated Silicon Nanoparticles," *Chemistry of Materials,* vol. 18, no. 26, pp. 6139-6146, Dec 26 2006.

[88]   K. Kusova *et al.*, "Luminescence of free-standing versus matrix-embedded oxide-passivated silicon nanocrystals: The role of matrix-induced strain," *Appl. Phys. Lett.,* vol. 101, no. 14, Oct 1 2012.

[89]   W. Fang, E. Simoen, M. Aoulaiche, J. Luo, C. Zhao, and C. Claeys, "Distinction between silicon and oxide traps using single-trap spectroscopy," *Physica Status Solidi A: Applied Research,* vol. 212, no. 3, pp. 512-517, Mar 2015.

[90] D. Jurbergs, E. Rogojina, L. Mangolini, and U. Kortshagen, "Silicon Nanocrystals with Ensemble Quantum Yields Exceeding 60%," *Appl. Phys. Lett.,* vol. 88, no. 23, Jun 5 2006.

[91] Y. Yu, C. M. Hessel, T. D. Bogart, M. G. Panthani, M. R. Rasch, and B. A. Korgel, "Room temperature hydrosilylation of silicon nanocrystals with bifunctional terminal alkenes," *Langmuir,* vol. 29, no. 5, pp. 1533-1540, 2013.

[92] Z. Yang, M. Iqbal, A. R. Dobbie, and J. G. C. Veinot, "Surface-Induced Alkene Oligomerization: Does Thermal Hydrosilylation Really Lead to Monolayer Protected Silicon Nanocrystals?," *J. Am. Chem. Soc.,* vol. 135, no. 46, pp. 17595-17601, Nov 20 2013.

[93] H. Mizuno, H. Koyama, and N. Koshida, "Oxide-free Blue Photoluminescence from Photochemically Etched Porous Silicon," *Appl. Phys. Lett.,* vol. 69, no. 25, pp. 3779-3781, Dec 16 1996.

[94] M. Dasog *et al.*, "Chemical Insight into the Origin of Red and Blue Photoluminescence Arising from Freestanding Silicon Nanocrystals," *ACS Nano,* vol. 7, no. 3, pp. 2676-2685, Mar 2013.

[95] Y. Yu, C. E. Rowland, R. D. Schaller, and B. A. Korgel, "Synthesis and Ligand Exchange of Thiol-Capped Silicon Nanocrystals," *Langmuir,* vol. 31, no. 24, pp. 6886-6893, 2015/06/23 2015.

[96] N. B. Cramer, T. Davies, A. K. O'Brien, and C. N. Bowman, "Mechanism and Modeling of a Thiol-ene Photopolymerization," *Macromolecules,* vol. 36, no. 12, pp. 4631-4636, Jun 2003.

[97] Z. M. Rong, B. R. Henry, T. W. Robinson, and H. G. Kjaergaard, "Absolute intensities of CH stretching overtones in alkenes," *J. Phys. Chem. A,* vol. 109, no. 6, pp. 1033-1041, Feb 2005.

[98] F. Meinardi *et al.*, "Highly Efficient Luminescent Solar Concentrators Based on Earth-abundant Indirect-bandgap Silicon Quantum Dots," *Nat. Photonics,* vol. 11, pp. 177-185, 02/20/online 2017.